

High S/N Echelle Spectroscopy in Young Stellar Groups [★]

II. Rotational Velocities of Early-Type Stars in Sco OB2

A.G.A. Brown^{@1}, W. Verschueren^{@2,1}

^{@1} Sterrewacht Leiden, P.O. Box 9513, 2300 RA, Leiden, The Netherlands ^{@2} University of Antwerp (RUCA), Astrophysics Research Group, Groenenborgerlaan 171, 2020 Antwerpen, Belgium

Received... , accepted...

Abstract. We investigate the rotational velocities of early-type stars in the Sco OB2 association. We measure $v\sin i$ for 156 established and probable members of the association. The measurements are performed with three different techniques, which are in increasing order of expected $v\sin i$: 1) converting the widths of spectral lines directly to $v\sin i$, 2) comparing artificially broadened spectra of low $v\sin i$ stars to the target spectrum, 3) comparing the He I $\lambda 4026$ line profile to theoretical models. The sample is extended with literature data for 47 established members of Sco OB2. Analysis of the $v\sin i$ distributions shows that there are no significant differences between the subgroups of Sco OB2. We find that members of the binary population of Sco OB2 on the whole rotate more slowly than the single stars. In addition, we find that the B7–B9 single star members rotate significantly faster than their B0–B6 counterparts. We test various hypotheses for the distribution of $v\sin i$ in the association. The results show that we cannot clearly exclude any form of random distribution of the direction and/or magnitude of the intrinsic rotational velocity vector. We also investigate the effects of rotation on colours in the Walraven photometric system. We show that positions of B7–B9 single dwarfs above the main sequence are a consequence of rotation. This establishes the influence of rotation on the Walraven colours, due primarily to surface gravity effects.

Key words: stars: early-type; formation; rotation – open clusters and associations: individual: Sco OB2

1. Introduction

An outstanding problem in theories of star formation is the so-called angular momentum problem. Molecular clouds and cloud cores, even if they spin about their axis only once per Galactic rotation, contain much more angular momentum than the stars that form from them (see e.g., Spitzer 1968). Observations suggest that an interstellar parent cloud must lose at least two to four orders of magnitude of angular momentum for a relatively wide binary system and a single star, respectively, to become dynamically possible (see Mouschovias 1991). How does angular momentum get redistributed when stars form and what is the resulting distribution of rotational velocities? These questions can best be addressed by studying young stellar groups in which the stars are unevolved and physically related. It is in these groups that the observed distribution of projected rotational velocities ($v\sin i$) may still reflect the distribution of rotational velocities at the time of star formation. Observations of the present $v\sin i$ distribution provide constraints on the angular momentum history of forming stars, and contain information on mechanisms that lead to angular momentum redistribution during star formation.

Suggested mechanisms for the redistribution of angular momentum, include magnetic braking and the formation of disks. Magnetic braking is important during the early, diffuse stages of star formation (Mouschovias 1991). Stellar disks are important during the proto-stellar and pre main-sequence phases (see e.g., Bodenheimer et al. 1993). Another way of redistributing angular momentum during star formation is through the formation of binary systems. This mechanism can be studied by relating the characteristics of the binary population in stellar groups to the $v\sin i$ distribution, which may also provide information about tidal interactions in close binaries. Ultimately, observations of the $v\sin i$ distribution in young stellar groups may provide information on the star formation process it-

Send offprint requests to:

A.G.A. Brown, brown@strw.leidenuniv.nl

[★] Based on observations obtained at the European Southern Observatory (ESO), La Silla, Chile in the framework of Key Programme 5-005-45K

arXiv:astro-ph/9608089v1 14 Aug 1996

self. For a recent review on the role of rotation in star formation, see Bodenheimer et al.(1993).

Another important aspect of the study of rotational velocities of stars is the effect of rotation on observed stellar parameters. It is well known that photometry and spectral classification of stars are affected by rotation, due to surface gravity effects. The resulting misinterpretation of the observed stellar parameters will bias age determinations for stellar groups and the derived mass distributions (e.g., Maeder 1971).

OB associations are young and mostly unobscured sites of recent star formation and as such are well suited for studies of the properties of young groups of stars (for reviews see Blaauw 1964, 1991). In this paper we focus on the Sco OB2 association. Because of its proximity (the distance to Sco OB2 is ~ 145 pc, see de Geus et al. 1989) it is easily accessible to proper motion studies and as a result extensive membership determinations have been carried out for this association. Sco OB2 consists of three well-known subgroups; Upper Scorpius (US), Upper Centaurus Lupus (UCL) and Lower Centaurus Crux (LCC). The Upper Scorpius subgroup is located near the remnants of its parental molecular cloud, and some of its stars are still partly obscured by gas and dust. We also study a subgroup located southeast of US, although the physical reality of this subgroup has never been established.

The ages of the three main subgroups were determined most recently from Walraven photometry by de Geus et al.(1989). They found ages of 4–5 Myr, 14–15 Myr and 11–12 Myr for US, UCL and LCC, respectively. For US the kinematic age (i.e., the age determined by tracing the proper motions of the members back in time) was determined by Blaauw (1978, 1991) to be 5 Myr.

Studies of rotational velocities in Sco OB2 have in the past concentrated mainly on US. Slettebak (1968) determined $v \sin i$ for 82 stars in US and UCL and found that on average the stars in US rotate faster than those in UCL (174 km s^{-1} vs. 119 km s^{-1} , but the rms spreads on these numbers are $\sim 100 \text{ km s}^{-1}$) and that the mean $v \sin i$ for B7–A0 stars is larger than that of corresponding field stars (212 km s^{-1} vs. 138 km s^{-1}). The B0–B6 stars were found to rotate somewhat more slowly than field stars. Rajamohan (1976) derived rotational velocities for 112 members of Sco OB2 and found that for stars with $M_V < 0^m0$ the distributions of rotational velocities are similar for US and UCL and resemble those of field stars. Stars with $M_V > 0^m0$, all of which are located in US, were found to rotate much faster than corresponding field stars.

In this paper we present new projected rotational velocities from high-resolution spectra for stars that are established or probable members of the Sco OB2 association. We briefly describe the observations and sample selection in Sect. 2. In Sect. 3 we present and discuss the different techniques used to derive $v \sin i$ from the observed spectra. In Sect. 4 we discuss the observed distribution of pro-

jected rotational velocities. Various hypotheses about the true distribution of rotational velocities are tested for the known members of Sco OB2. We also discuss the interpretation of the data in the context of these hypotheses. In Sect. 5 we combine photometric data with our rotational velocities and confirm that rotation affects the colours of the stars in the Walraven photometric system. We discuss the effects of the colour changes on age determinations and derivations of mass distributions. Finally, in Sect. 6 we summarize our conclusions and suggest future work.

2. Observations

The spectra from which the projected rotational velocities are derived were all obtained with the ECHELLE + Electronographic Camera (ECHELEC) spectrograph, mounted at the Coudé focus of the ESO 1.52m telescope at La Silla. It consists of a 31.6 grooves/mm echelle grating and a 632 grooves/mm grism as a cross-disperser. The detector was a CCD (thinned, back-illuminated, RCA) with 640×1024 pixels of $15 \times 15 \mu\text{m}^2$, and a read-out noise of 65 e^- . In order to increase the signal to noise on read-out the CCD pixels were binned 2×2 (henceforth any reference to CCD-pixels is to the binned pixels). The linear dispersion of ECHELEC is 3.1 \AA/mm at 4000 \AA as measured for our data. This implies a velocity scale of 7 km s^{-1} per binned pixel and a resolving power of 21 500. The spectra cover the wavelength region 3800–4070 \AA which was recorded in 11–12 spectral orders. The formal (i.e., taking only photon and read-out noise into account) signal to noise ratio, measured at the top of the blaze profile in each order, typically varies from ~ 70 to ~ 300 between the blue and the red end of the spectrum. Further details on the observations are given in Verschueren et al.(1996), which also describes the data reduction procedure in detail.

The data were collected during 1991–1993 in the framework of an ESO Key Programme aimed at the determination of high-precision radial velocities of early-type stars in young stellar groups (Hensberge et al.1990). The stars that were observed are established or probable members of Sco OB2. They form a subset of a larger sample of stars that was submitted for observation by the HIPPARCOS satellite. The details of the selection of the HIPPARCOS sample can be found in de Zeeuw, Brown & Verschueren (1994). For the present study a total of 156 stars was observed, of which 136 already have a measured $v \sin i$. We note here that the observations were not specifically designed for rotational velocity studies. The aim was to gather radial velocities and also to observe stars repeatedly in order to detect possible spectroscopic binaries. However, the data are also well suited for deriving a large and homogeneous set of rotational velocities. Because of telescope and instrumental limitations the magnitude limit of our sample is $\sim 7^m5$. As a result 75% of the stars in our sample are of spectral type earlier than B7 (see also Verschueren et al.1996).

Of the observed sample 74 stars are established members, inferred from proper motions, found by Blaauw (1946) and Bertiau (1958). For 13 stars membership was inferred from photometry by de Geus et al. (1989). For the analysis in Sects. 4 and 5 we also added $v \sin i$ data from the literature (Slettebak 1968, and Uesugi & Fukuda 1981) for 47 established members which were not observed in our programme. Of these additional stars, 36 are proper motion members, the remaining ones are photometric members. Our observed sample is divided among spectral type as follows: 2 O stars, 93 B0–B3 stars, 22 B4–B6 stars, 25 B7–B9 stars and 14 A–F stars. The additional data from the literature consists of 6 B0–B3 stars, 8 B4–B6 stars, 32 B7–B9 stars and 1 A star. In addition to stars in Sco OB2 8 early-type stars were observed which are not related to the association. A number of these stars were used in the process of deriving $v \sin i$ (see Sect. 3.2). The data were collected during four observing runs. The runs are labeled E2, E3, E5 and E7 by Verschueren et al. (1996); we will use these labels here as well.

3. Techniques Used to Determine $v \sin i$

We have used three different methods to obtain $v \sin i$ from the ECHELEC spectra for the stars in our sample:

1. Deriving $v \sin i$ from the full-width half-maximum (FWHM) of weak metal lines. This method is applicable for $v \sin i \lesssim 80 \text{ km s}^{-1}$.
2. Deriving $v \sin i$ from the comparison between an artificially broadened sharp-lined template spectrum and the spectrum of a star for which $v \sin i$ is to be determined. This method is potentially applicable for $50 \text{ km s}^{-1} \lesssim v \sin i \lesssim 200 \text{ km s}^{-1}$. This range depends on spectral type (see Sect. 3.2 and Appendix C).
3. Deriving $v \sin i$ from the comparison of theoretical line profiles for the He I $\lambda 4026$ line with the observed line profile. The theoretical profile is taken from atmosphere models for rotating early-type stars by Collins et al. (1991, hereafter CTC). This method is in principle applicable for all velocities but is most useful for velocities for which method 2 fails, specifically for higher $v \sin i$.

Methods 1 and 2 rely on the classical model for rotating stars, as presented e.g., in Chapt. 2 of Tassoul (1978). The third method relies on theoretical models in which the line profiles are calculated *ab initio*. Recently Collins & Truax (1995) discussed the consequences of using the classical model rather than the physically more appropriate *ab initio* model. The most important point Collins & Truax make is to beware of the assumptions that underlie the classical model for rotating stars. These are:

- A. The observational aspect of a uniformly rotating star may be approximated by a circular disk subject to a

limb-darkening law applicable to all parts of the stellar disk.

- B. The limb-darkening law and coefficient appropriate for the radiation in a line are the same as for the continuum.
- C. The form of a line does not change over the apparent disk; it is simply uniformly Doppler-shifted by the radial motion resulting from rotation.

Assumption A means that the radial velocity is constant along lines parallel to the meridian plane of the star. This assumption breaks down at high rotational velocities where the surface of the star starts to deform and can no longer be described as a sphere. The effects of the deformation of the star are twofold. The lines of constant radial velocity are not parallel to the meridian plane of the star and the line formation process is influenced.

The second assumption, B, is flawed for the following reason. The limb-darkening law describes the variation of the specific emergent intensity from the centre of the stellar disk to the limb. The limb-darkening laws that are usually quoted in the literature are derived for the continuum. However, because the core of a line has a lower specific intensity at the centre of the stellar disk, the total variation from centre to limb of the intensity at the wavelength of the line-core will be less. Hence the limb-darkening coefficient will be smaller for the line-core. This effect is very important in strong lines, where the limb-darkening coefficient shows a variation from the continuum through the wings to the core.

Assumption C does not hold at high rotational velocities because the distortion of the star introduces variations in the ionization-excitation equilibrium over the surface of the star. Furthermore, the local form of the line is influenced by gravity darkening and shape distortion. This means that there is a difference between the line profiles of an intrinsically slow rotator and those of a fast rotator seen pole-on. However, according to calculations in Collins & Truax (1995) the differences are very small and of no concern to the determination of $v \sin i$.

Before discussing the three methods in detail we should mention the format of the spectra. After the data reduction process the spectra are in the form of normalized flux as a function of CCD-pixel. The pixel scale has to be converted to a wavelength scale and for the radial velocity studies a log-wavelength scale is used (see Verschueren et al. 1996). It turns out that due to the specific geometry of the ECHELEC instrument, the CCD-pixel spacing in the spectra is almost identical to a spacing in $\ln \lambda$. For methods 1 and 2 we used spectra that were not yet converted to $\ln \lambda$ -space and for which the different echelle orders were not merged. Furthermore, the continuum of the spectra was not yet globally corrected for instrumental effects (such as the echelle blaze), which means we had to use a local continuum for method 1. For method 3 we only used the order containing the He I $\lambda 4026$ line, and to

facilitate the comparison of the data to the model profiles the order was rebinned into $\ln \lambda$ -space. In the rebinned spectra the spacing is 2.8×10^{-5} in $\ln \lambda$ or 8.4 km s^{-1} .

3.1. Deriving $v \sin i$ for Sharp-Lined Stars

If one assumes that spectral lines in a star are broadened by rotation only, the width of the lines can be used to derive $v \sin i$. In practice spectral lines are also broadened by thermal and instrumental effects and by other mechanisms, such as the Stark effect (see e.g., Gray 1992, Chapt. 17). Therefore one should use weak metal lines that are in principle only affected by thermal and instrumental broadening; two effects one can correct for. However, the weak metal lines can also be broadened due to blending, the possible spectroscopic binary nature of the star, or curve of growth effects. The latter is important for some of the stars in our sample (see below). Possible spectroscopic binaries show obvious double lines or they reveal themselves as stars for which $v \sin i$ changes from one observing run to the other. Neglecting the binary nature leads to over-estimates of $v \sin i$. The presence of line blends is more or less automatically taken care of in the conversion of line-widths to $v \sin i$ described below.

At low values of $v \sin i$ one has to take into account the consequences of assumptions B and C. Because the lines we use are intrinsically narrow and weak (the median residual flux in the line cores is $\sim 94\%$, the average and rms spread being $\sim 91\%$ and $\sim 8\%$) the limb-darkening parameter will not be very different from the continuum limb-darkening parameter. The small wavelength range of the ECHELEC spectra also ensures that the limb-darkening parameter is nearly constant over the entire spectrum.

The widths of the metal lines are measured by fitting a Gaussian plus a straight-line (pseudo) continuum to the spectral line. As much continuum as possible is used and where necessary double Gaussians are fitted. The fitting process returns the FWHM of the best fitting Gaussian, which is a measure of the second moment of the line profile. The second moments for different limb-darkening laws are derived in Appendix A; because of our CCD-pixel-spacing we use the formulas for $\ln \lambda$ -spacing. Note that Collins & Truax (1995) give the half-width at half-maximum instead of the FWHM. The formal errors on the derived FWHM and amplitude of the best fitting Gaussian vary between $\sim 1\%$ and $\sim 40\%$. These errors are influenced by uncertainties in the continuum level and a line-depth (at line-centre) of at least 4–5% is required if both the FWHM and amplitude of the best fitting Gaussian are to have errors of less than 5%.

The broadening of the lines depends on the assumed limb-darkening law. We used a linear limb-darkening law to relate the line-widths to $v \sin i$. Díaz-Cordovés et al. (1995) give limb-darkening parameters for the linear, quadratic and square-root approximations to limb-

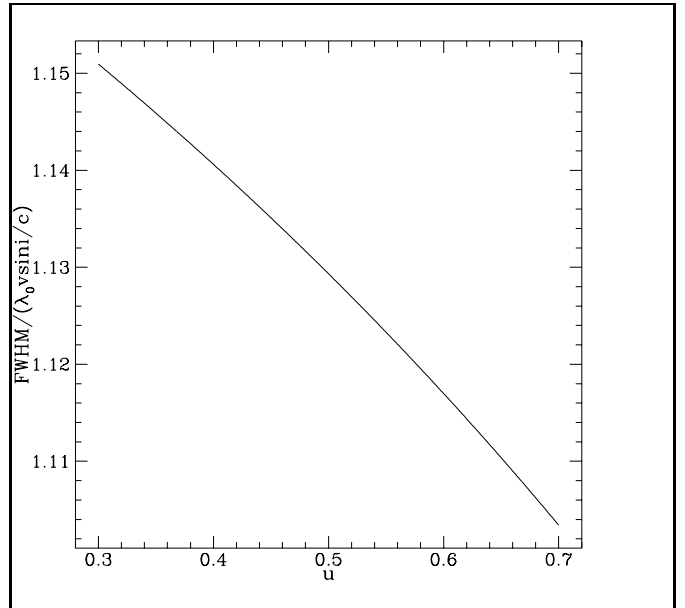


Fig. 1. The value of the FWHM of an infinitely sharp line which has been broadened by rotation as a function of the linear limb-darkening parameter u . The full-width-half-maximum is normalized by $\lambda_0 \frac{v \sin i}{c}$ (see Appendix A).

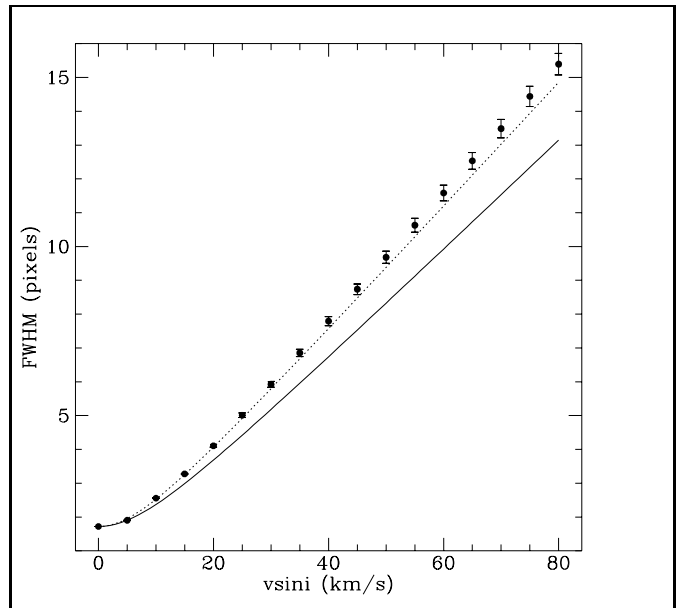


Fig. 2. Analytically calculated FWHM of spectral lines (solid curve) vs. the FWHM found by fitting a Gaussian (dots). The results are shown as a function of $v \sin i$ for an instrumental profile of 1.4 pixels FWHM, a thermal broadening of 1 pixel FWHM and $u = 0.4$. The dotted line shows the result of fitting $\text{FWHM} = \sqrt{a^2 + b^2(v \sin i)^2}$ to the dots. The fit is determined primarily by the points at low $v \sin i$. The error at high $v \sin i$ values amounts to 4% at most.

darkening. Their values are based on Kurucz (1991) atmosphere models. The value of the limb-darkening parameter

for the linear law varies from ~ 0.3 to ~ 0.7 for the range of spectral types in our sample. We chose a constant value of 0.4 (characteristic of spectral type B3–B5, which is in the middle of our range) to derive $v \sin i$ from the line-widths. Figure 1 shows the variation of the FWHM as a function of the limb-darkening parameter. It is clear from the figure that only small errors are made when using a single value for u . The variation between the extreme values is $\sim 4\%$.

The measured line-widths also contain contributions from instrumental and thermal broadening. These contributions have to be subtracted before $v \sin i$ is derived. For our spectra, the instrumental broadening amounts to 1.4 CCD-pixels FWHM for run E5 and 1.6 pixels for the other runs. These values were derived from the measured widths of thorium lines in the wavelength calibration spectra. The only metal lines that experience any significant thermal broadening (as compared to the instrumental FWHM) are the C, N and O lines. The amount of thermal broadening in these lines varies from ~ 0.7 –1.4 pixels FWHM. We divided our spectral range roughly into three temperature ranges. For stars with temperatures around $T_{\text{eff}} = 8000$ K an average thermal profile of 0.7 pixels FWHM is used. For $T_{\text{eff}} = 15000$ K and $T_{\text{eff}} = 25000$ K the values are 0.9 and 1.2 pixels FWHM. The differences are small, but they are important for the stars with the sharpest lines. In practice the spectral type ranges that correspond to the temperatures above are: A1–B9, B8–B4, and B3–B0, respectively.

Table 1. Values of parameters a^2 and b^2 .

T_{eff}	E2/E3/E7		E5	
	a^2	b^2	a^2	b^2
8000 K	3.05	3.40×10^{-2}	2.45	3.35×10^{-2}
15000 K	3.37	3.40×10^{-2}	2.77	3.39×10^{-2}
25000 K	4.00	3.39×10^{-2}	3.40	3.40×10^{-2}

The fitting of Gaussians to estimate the line-widths introduces a bias because of the non-Gaussian form of the rotational broadening function. We have determined this bias by making artificially broadened Gaussian lines that had intrinsic widths corresponding to instrumental plus thermal broadening. The Gauss-fitting routine was applied for a range of $v \sin i$ values and the results were represented with a function of the form $\text{FWHM} = \sqrt{a^2 + b^2(v \sin i)^2}$. The parameters a^2 and b^2 are then used in the derivation of $v \sin i$. Figure 2 shows an example of this investigation. The FWHM values found with the Gauss-fitting routine are compared to the analytically calculated values (Appendix A). The values for a^2 and b^2 are listed in Table 1 for different stellar temperatures for observing runs E2/E3/E7 and E5 separately.

Finally, to convert the widths of metal lines to $v \sin i$ the following procedure is used. The widths are measured

for as many lines as possible (typically 10–50, depending on $v \sin i$ and spectral type) and converted to a histogram of $v \sin i$ values for each star. This histogram will be contaminated by line-blends as well as by interstellar lines. By selecting the bins where most of the $v \sin i$ values are concentrated one can weed out the blended lines, which cause $v \sin i$ to be overestimated, and interstellar lines, which lead to underestimates. This method has been used before by Day & Warner (1975). In practice it works best for sharp lined stars with a large number of lines. One can then easily distinguish a peak in the histogram. Examples are shown in Fig. 3 for two stars. One is a sharp-lined A1V star ($v \sin i = 7 \text{ km s}^{-1}$) for which ~ 130 lines were measured. The other is a B2V star rotating with $v \sin i \approx 60 \text{ km s}^{-1}$, and for which 25 lines were measured. Also shown is the FWHM vs. line-strength for all lines measured. The lines that correspond to the peaks in the histograms are indicated as solid circles. Note that these lines define a definite locus and that for these two examples there is no increase of the FWHM with line-depth. All other lines are either blends, interstellar, or affected by cosmic rays. In the case of HD 144218 the value of $v \sin i$ is higher and the peak in the FWHM distribution is less well defined.

Once the most likely range for $v \sin i$ has been selected from the histograms we proceed by checking whether there is a significant correlation between line-depth and FWHM. Such a correlation is expected if lines are on the flat part of the curve of growth, where the FWHM increases with line-depth. If a significant correlation is found we correct the FWHM of each line by fitting a linear model to the data. After this correction we check whether the distribution of the FWHM of the lines is significantly skewed towards high values. If this is the case there may still be line blends in the data. We correct for these blends by repeatedly discarding the line with the largest FWHM until the rms spread in the data changes by no more than 10%. This procedure is applied subject to the condition that no more than 30% of the lines are discarded. The two quantitative criteria were found by trial and error. After the selection procedure is completed $v \sin i$ is calculated as a weighted average of the $v \sin i$ values given by each line. In order to ensure that lines with erroneously low formal errors on their FWHM do not enter into this average with too much weight, the median error in the FWHM is calculated from the data and half of this value is added in quadrature to all errors.

3.2. Deriving $v \sin i$ by Template Broadening

For stars with $v \sin i$ larger than about 50 km s^{-1} the method for deriving $v \sin i$ described above becomes unreliable. This is because the estimated stellar continuum level is already significantly too low due to rotational broadening, which implies that the measured FWHM of the lines is underestimated. Furthermore, at higher values of $v \sin i$

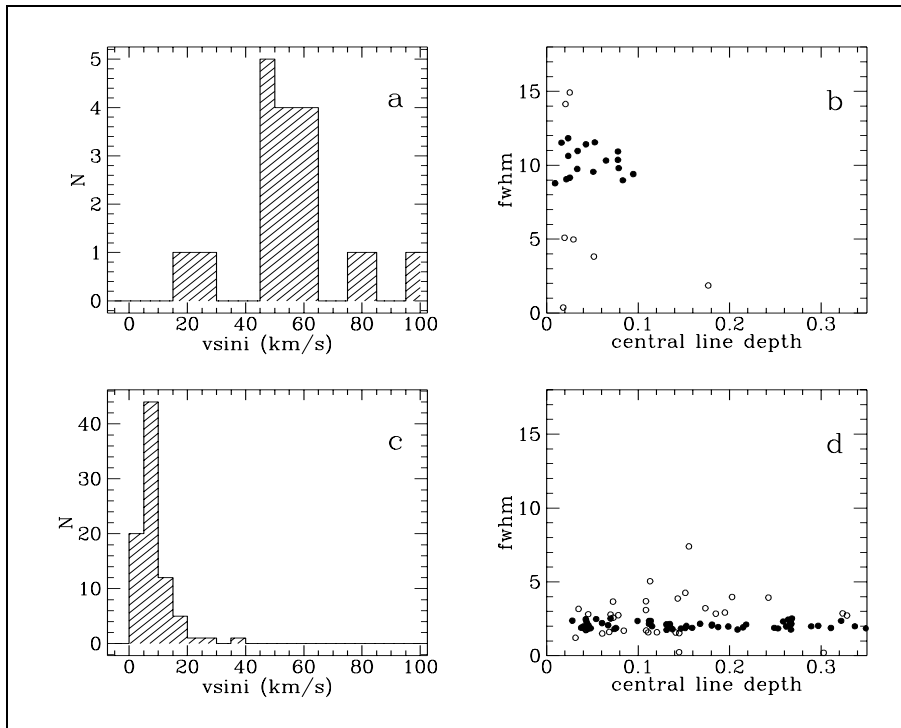


Fig. 3. Histograms of $v \sin i$ values derived from measured line-widths and the line-widths vs. line-strengths. The data for HD 144218 (B2V) are shown in (a) and (b). The data for HD 72660 (A1V) are shown in (c) and (d). Indicated with solid circles are the lines corresponding to the peaks in the histograms. For HD 144218 this is the velocity range $45 \text{ km s}^{-1} \leq v \sin i \leq 65 \text{ km s}^{-1}$ and for HD 72660 the range is $0\text{--}10 \text{ km s}^{-1}$ (the sharpest lines in HD 72660 formally give negative $v \sin i$ values, after subtraction of thermal and instrumental broadening, and are either interstellar, or affected by cosmic rays, or under-sampled).

the number of lines for which one can measure the FWHM is reduced, and it is more difficult to identify and eliminate line blends. Therefore, a different technique for obtaining $v \sin i$ is required.

The technique we consider here is that of broadening of spectra of sharp-lined stars and comparing the broadened spectrum to the spectrum of the target star for which $v \sin i$ is to be determined. Again, the model that is used when broadening a template spectrum is the classical model for rotating stars. In this case all three assumptions of the classical model play a role. The assumptions on limb-darkening are now very relevant because of the inclusion of broad and strong hydrogen and helium lines in the determination of $v \sin i$. The limb-darkening we used was again linear limb-darkening with a parameter $u = 0.4$. The effects of varying the limb-darkening are discussed at the end of Appendix C. At the highest $v \sin i$ values the deformation of the target star, which leads to changes in line-shapes over its surface, shows up as a mismatch between its spectrum and the broadened template spectrum (see also Appendix C). The template stars were taken from our own sample and they were required to have a low value of $v \sin i$ ($\sim 10\text{--}20 \text{ km s}^{-1}$), which was determined using method 1.

Bearing all the mentioned caveats in mind we proceed as follows. We broaden a template spectrum for a number of values of $v \sin i$ over a chosen interval and find the value for which the difference between broadened template and target is minimal. The search interval is chosen based on the literature value for $v \sin i$ or by visual inspection of the spectrum of the target. The comparison between

the broadened template spectrum and the target spectrum is done for 10 orders in the ECHELEC spectra (i.e., orders 139–148, see Verschueren et al.1996). To find the best $v \sin i$ value a figure of merit analogous to a χ^2 is constructed for each order separately. This figure of merit is the mean absolute difference, over all pixels, between the template and the target divided by the noise in the target spectrum. This is essentially an automation of the comparison that one would do by eye. Based on the values of the figures of merit a weighted average of the $v \sin i$ values found for each order is calculated. Values of $v \sin i$ at the edge of the search interval are discarded. These values usually point to noisy orders, orders with low information content or orders where there is a significant mismatch between the spectra of the template and the target. In all cases the values of $v \sin i$ found for all orders are inspected to check whether the results are consistent. The wrong choice for the search interval can cause a large spread in the data that is not real.

The advantage of doing the comparison per spectral order is that it provides information on $v \sin i$ independently for different parts of the spectrum. This provides an effective way of detecting mismatches, either intrinsic or due to the data reduction process, between the template and target spectra by demanding consistency of $v \sin i$ values. A global comparison only gives a single value of $v \sin i$ and spectral type mismatches are then only revealed by visual inspection. Furthermore, from the spread in the data and a visual inspection of the results one gets a good indication of the precision as well as the accuracy with which $v \sin i$ was determined. Finally, there are often weaker lines

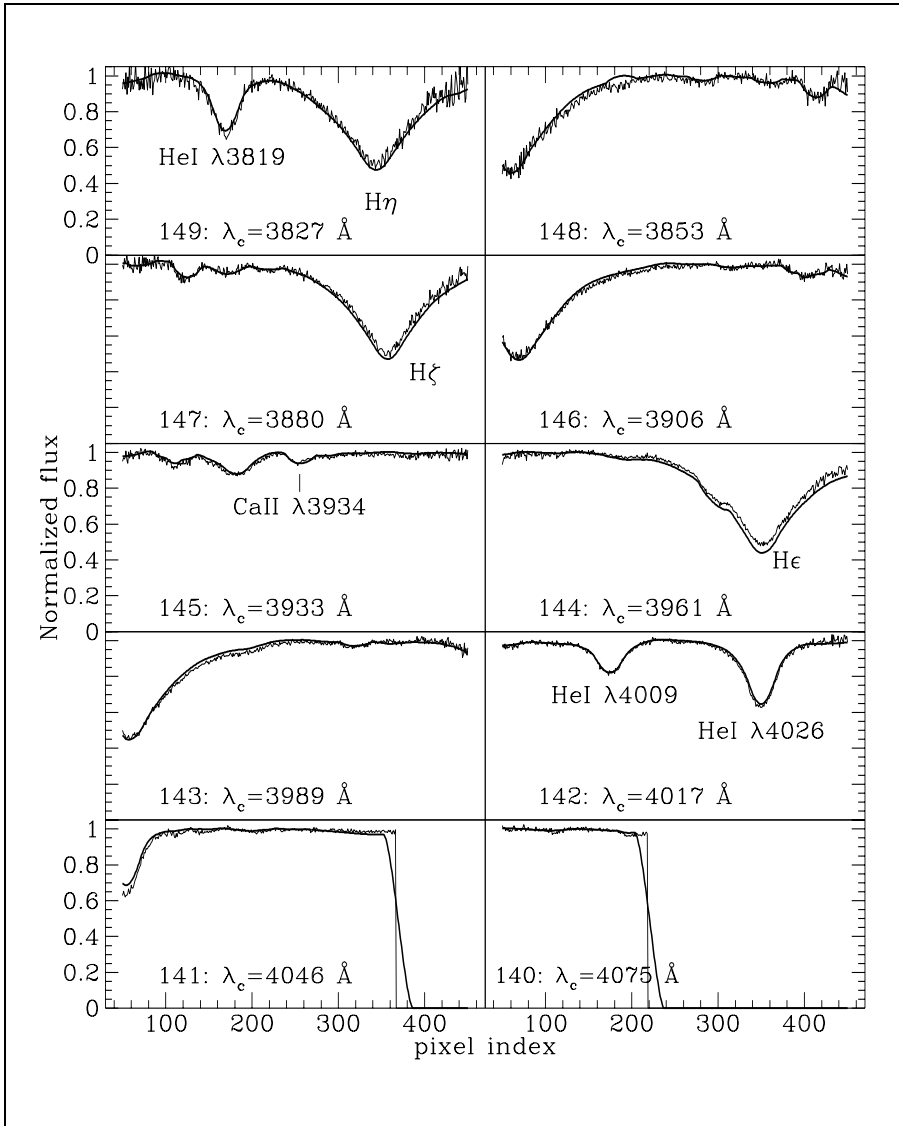


Fig. 4. Comparison of the target spectrum of HD 121790 (B2IV-V) with the best-fit broadened template spectrum of HD 96706 (B2V). The thick line is the broadened template spectrum. The central wavelength of each order is indicated, as well as several spectral lines. The best value of $v \sin i$ for the target star is 118 km s^{-1} . Note the mismatches between the spectra of the stars at several places in the continuum as well as in the wings of the hydrogen lines. These mismatches can be due to intrinsic spectral type mismatches or due to the data reduction process.

present in the broad wings of the Balmer lines. The influence of these lines is not taken into account in the models by CTC. These lines can make a difference if they are strong enough and template broadening automatically takes their contribution into account.

Spectral type mismatches often result from slight differences in temperature or luminosity class. The temperature differences are readily apparent in the strength of the helium lines for B-stars and the luminosity differences are manifest in the hydrogen lines. Another problem to take into account when looking for a template spectrum is a possible error in spectral classification of either template or target. The only way to get around this problem is to try different template spectra and find the best match.

The information on $v \sin i$ in the rotationally broadened spectra resides in the metal lines and in central parts of hydrogen and helium lines. It is important to get rid of the continuum and of the broad wings of Stark-broadened lines when calculating the figure of merit, otherwise these

components dominate the determination of $v \sin i$, whereas in practice they carry no information on $v \sin i$. This problem can be solved by high pass filtering both spectra before comparing them. The filtering is done with a high-pass frequency filter in Fourier-space. The details of the filtering process are given in Appendix B.

Figures 4 and 5 show an example of the fitting process for a star for which the best value of $v \sin i$ is 118 km s^{-1} . It is HD 121790, a B2IV-V, star and the template is HD 96706 with spectral type B2V. Figure 4 shows a direct comparison of the broadened template and the target spectrum. Figure 5 shows a comparison of the Fourier filtered spectra. All spatial wavelengths longer than 358 km s^{-1} were filtered out in this case. Note that in Fig. 4 there are several mismatches between the two spectra in the continuum as well as in the wings of the hydrogen lines. These mismatches bias the determination of $v \sin i$ if no filtering is applied. The comparison between the two filtered spectra shows convincingly that the broad-

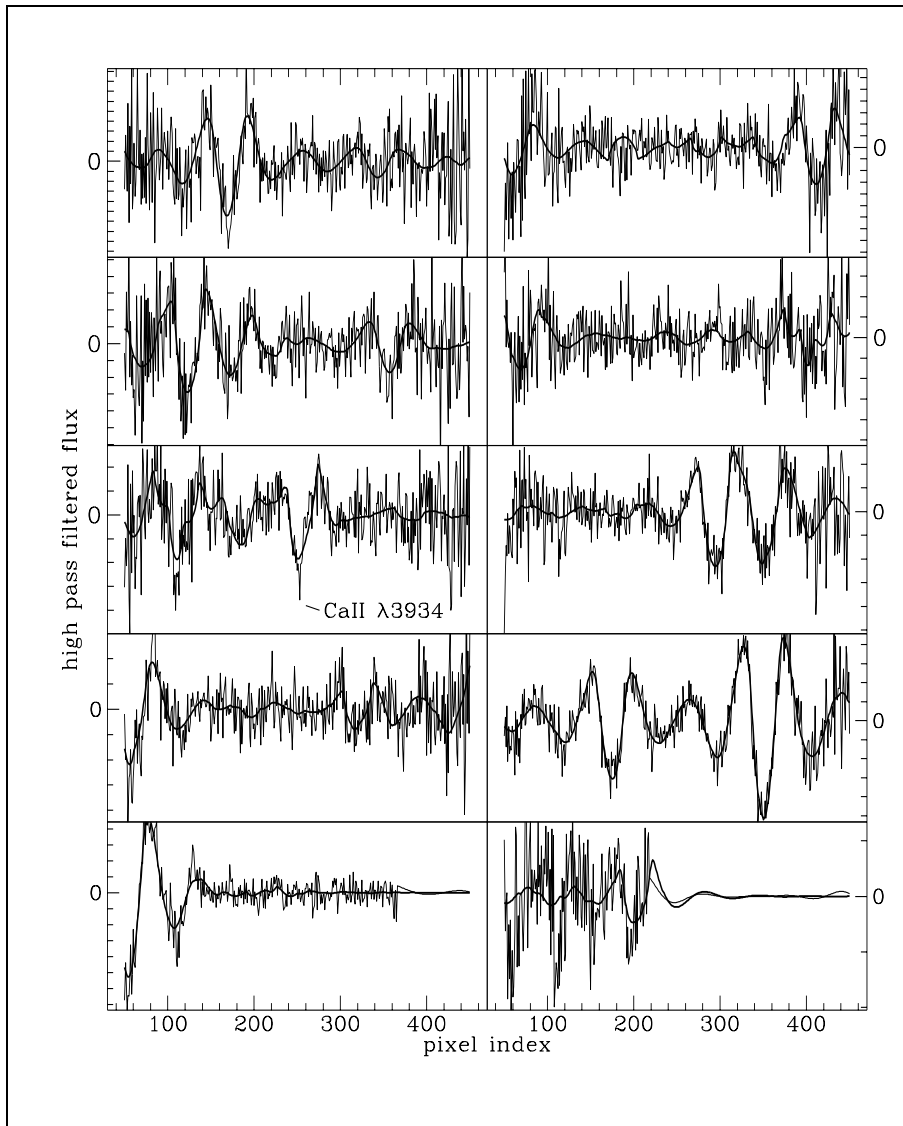


Fig. 5. The same as Fig. 4 but now for the high-pass filtered spectra. The order numbers and central wavelengths are the same as in Fig. 4. The distance between the tick-marks on the vertical scale is 0.01. The high-pass filter takes out all spatial wavelengths longer than 358 km s^{-1} (see also appendix B). Notice the very good fit of the two spectra.

ened template spectrum fits the target spectrum. The interstellar CaII $\lambda 3934$ line is located in the central part of order 145. This line is left out of the comparison between the spectra.

As mentioned in the beginning of this section, the template broadening technique fails at high values of $v \sin i$. The reason is that the classical model for rotational broadening does not take the effects of gravity darkening into account. For stars rotating at a large fraction of their break-up velocity the surface gravity decreases in the equatorial regions. This leads to obscuration of the parts of the observed line profile that come from the equatorial regions. The result is that rapidly rotating stars which are observed equator-on have line profiles that resemble those of more slowly rotating stars. Furthermore, because of the strong lines that are used we expect the effects of limb-darkening to be more severe. We investigated both these effects on the template broadening method by using synthetic data generated from the models by CTC. These investigations

are described in Appendix C. The conclusions are that the choice of the limb-darkening law is not important for template broadening, but gravity-darkening is important and one should be careful when using template broadening results as soon as $v \sin i$ is larger than $\sim 120\text{--}150 \text{ km s}^{-1}$.

3.3. Determining $v \sin i$ for Rapid Rotators by Model Fitting

For the stars with the highest values of $v \sin i$ one is only left with the alternative of comparing model line profiles to the data. The only line in our spectrum for which rotating stellar models have been calculated is the HeI $\lambda 4026$ line. The models are given by CTC for a set of values of w , the fraction of the critical angular velocity at which the star rotates, and i , the inclination angle of the rotation axis with respect to the line of sight. The critical angular velocity of the star corresponds to the equatorial rotational velocity at break-up. The models were calcu-

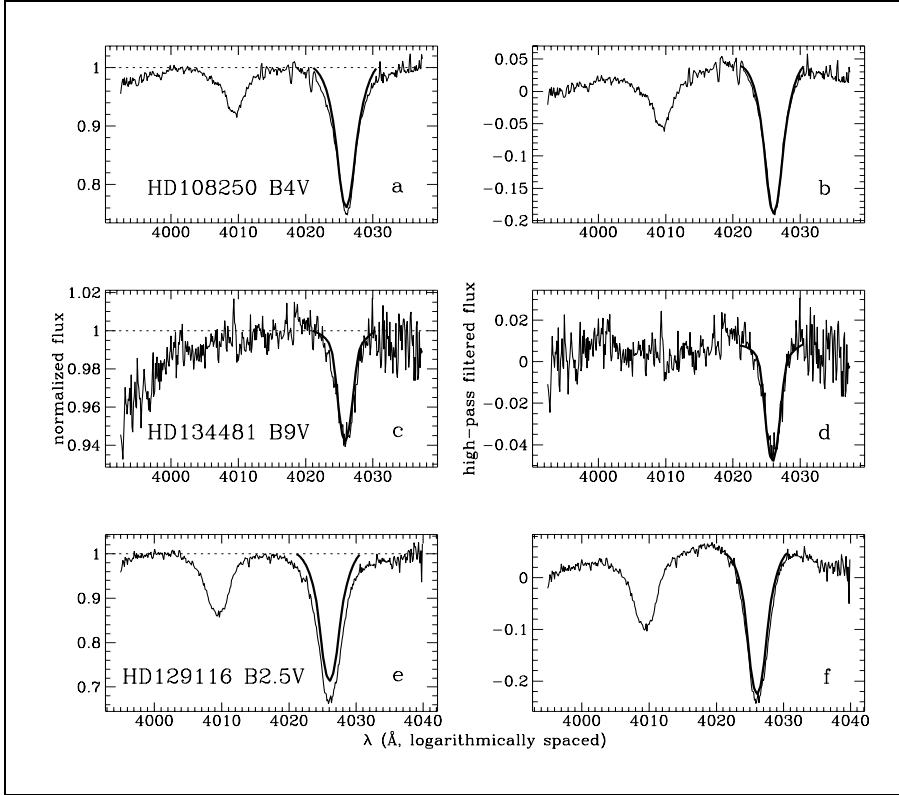


Fig. 6. Three examples of the model fitting process for deriving $v \sin i$. Figure (a) shows a direct comparison of the best fitting model (thick line; $w = 0.6$, $i = 50^\circ$, $v \sin i = 130 \text{ km s}^{-1}$) and the data for HD 108250. Figure (b) shows the same as (a) after high-pass filtering. Figures (c) and (d) show the same as (a) and (b) for HD 134481. The best fitting model in this case is: $w = 1.0$, $i = 30^\circ$, $v \sin i = 174 \text{ km s}^{-1}$. Figures (e) and (f) show the same as (a) and (b) and illustrate the effect of using a B3 model to fit the data of a B2 star. The He I $\lambda 4026$ line is weaker for B3 stars than for B2 stars and the effect is that $v \sin i$ is underestimated. The best fitting model in this case is: $w = 0.5$, $i = 60^\circ$, $v \sin i = 124 \text{ km s}^{-1}$. The dashed lines indicate the continuum level of the models and illustrate the need for high-pass filtering.

lated for main sequence stars and for stars of luminosity class III for the spectral types B1, B3, B5, B7, and B9. The CTC models are based on the Roche model described in Collins (1963, see also Sect. 4.2). The basic procedure we follow is to compare the whole line profile to the data for each (w, i) combination and determine $v \sin i$ from the best fitting models. We stress here that we cannot derive w and i separately with our data. Usually a number of (w, i) combinations are consistent with the data and one can only derive $v \sin i$ with a corresponding range of uncertainty.

From the set of models given by CTC we constructed a grid of models for each spectral type. In this grid w varies from 0 to 1.0 in steps of 0.1 and i varies from 0° to 90° in steps of 10° . The models at grid points not given by CTC were constructed by linear interpolation between CTC models. We verified that using higher order interpolation methods does not improve the model grid. We also constructed models for B4, B6 and B8 stars by linear interpolation between spectral types given by CTC. A similar procedure is not possible for B2 stars because they have the strongest He I $\lambda 4026$ lines; and here interpolation between B1 and B3 models is incorrect. For B2 stars B3 models were used and we discuss the implications below.

The model profiles are given as a function of wavelength so we used spectra rebinned into $\ln \lambda$ -space. The He I $\lambda 4026$ profiles were transformed to $\ln \lambda$ -space (spacing in $\ln \lambda$: 2.8×10^{-5}). The data and the models were compared for each (w, i) pair and the pair for which the re-

duced χ^2 is at a minimum was considered to correspond to the best fitting model. Possible radial velocity shifts were taken into account by automatically shifting the model with respect to the data for each (w, i) pair and searching for the minimum χ^2 .

In order to estimate the uncertainties in the derived value of $v \sin i$ the ten models with the lowest χ^2 were considered. Of these, a model was considered equivalent to the best fitting model if the associated χ^2 did not differ by more than a factor of 2 from the minimum and if the emergent flux at all points in the model did not differ by more than 0.01 for He I $\lambda 4026$ lines with a central depth of 0.9 or less. The maximum tolerated difference in fluxes was 0.005 for He I $\lambda 4026$ lines with a central depth of more than 0.9. The $v \sin i$ values corresponding to the best fitting models were subsequently averaged with the corresponding χ^2 values as weights. The rms spread in $v \sin i$ values was taken as the error bar. In some cases one finds only one best fitting model and then the adjacent points located between the grid points were considered in order to assign an error bar to $v \sin i$.

As was the case with template broadening, there may be mismatches between model and data due to the continuum. We turned to high pass filtering again to get around the continuum terms. Because one wants to compare the whole line profile to the data, and because most of the target stars have a high value of $v \sin i$, only the most important continuum terms should be filtered out. In order to safely examine stars with values for $v \sin i$ up to

500 km s⁻¹, we chose to filter away all spatial wavelengths larger than ~ 1000 km s⁻¹. None of the stars in our sample have $v \sin i$ values this high.

Figure 6 shows three examples of the model fitting process. In all cases the comparison between data and best fitting model is shown both for the high-pass filtered data and for the un-filtered data. In Figs. 6a and 6b the data for HD 108250 (B4V) are shown. The best fitting model is indicated by the thick line. Note that in the direct comparison it appears as if the He I $\lambda 4026$ model line is not deep enough and that the wings of the line profile do not match the data either. This is due to the continuum in the data which has not yet been properly rectified. This can be seen from Fig. 6b; the Fourier filtered model and data now match well in both the line core and in the wings. Figures 6c and 6d show the same for HD 134481 (B9V). In this case the continuum close to the He I $\lambda 4026$ line just happens to have the right value.

The strength of the He I $\lambda 4026$ line reaches a maximum around spectral type B2–B3 and the B3 models are not always strong enough compared to the data. This is often the case when one considers B2 stars. Figures 6e and 6f show the effects of using B3 models to fit the data for a B2 star (here HD 129116 B2.5V). The He I $\lambda 4026$ line is weaker in the B3 model than in the B2 star. Because both the broader wings and the deeper line core of the B2 star have to be fitted, $v \sin i$ is underestimated.

All results were inspected by eye to judge whether the best fitting model was actually correct. We encountered stars for which the models corresponding to their spectral types did not fit the data. In those cases other models were tried and the spectral type for which the best fit was obtained was used to derive $v \sin i$. For the majority of these cases the strength of He I $\lambda 4026$ and the ratio of He I $\lambda 4026$ to He I $\lambda 4009$ in our spectra indeed were not consistent with the spectral type of the star.

Finally, we remark that the $v \sin i$ values are based on the rotational velocity of the star at the theoretically calculated break-up velocity, and the value of w and i . This means that the later interpretation of $v \sin i$ distributions in terms of break-up velocities will be complicated (see Sect. 4).

3.4. Results

The results of the $v \sin i$ determinations are shown in Tables 2a–2d. The tables contain the following data. Column (1) gives the HD number of the star and column (2) gives the number of the star in the HIPPARCOS Input Catalogue (Turon et al.1992). In column (3) the spectral type is given as listed in the HIPPARCOS Input Catalogue. The derived value of the projected rotational velocity and its associated error are listed in columns (4) and (5). For stars for which we have $v \sin i$ values from different runs the error-weighted average is listed. For the following sharp-lined stars the $v \sin i$ values from two or more runs

are not consistent within the error bars: HD 109668, HD 110879, HD 120307, HD 122980, HD 132955, HD 133955, HD 145502, HD 147165, HD 158408, HD 172910. These stars all turn out to be spectroscopic binaries or radial velocity variables (see below). CTC provide a value for the break-up velocity (v_{br}) for each spectral type for which model profiles were calculated. Columns (6) and (7) list this break-up velocity and the ratio $v \sin i / v_{br}$. In cases where the CTC model profiles were used the value of v_{br} corresponds to the spectral type of the best fitting model and not necessarily to the listed spectral type (see also the notes to Table 2). For stars later than A0 and for supergiants we determined the break-up velocities based on stellar parameters given by Straižys & Kuriliene (1981) and Harmanec (1988). For HD 149757 and HD 151804 we took the mass and radius given by Lamers & Leitherer (1993). In column (8) we list which method was used to derive $v \sin i$. The method is indicated by its number and for some stars more than one method was used and a weighted average of $v \sin i$ was then formed. For a number of stars none of the methods for determining $v \sin i$ works (these are very early-type stars or late-type stars with only blended lines, or spectroscopic binaries for which line-profile fitting does not work). For these stars $v \sin i$ was estimated by visual inspection of the spectrum or by taking a literature value; as indicated in the notes. In column (8) this is indicated by the number 4. Column (9) indicates whether or not a star is a member of Sco OB2; 'm' indicates that the star is a photometric member, as found by de Geus et al.(1989), and 'M' indicates that the star is a proper motion member, as found by Blaauw (1946) and Bertiau (1958). Finally, in column (10) we list whether the star has a constant radial velocity (CON), is a radial velocity variable (RV), a single-lined spectroscopic binary (SB1) or a double-lined spectroscopic binary (SB2). For stars without an entry in column (10) there is no good information on their binarity.

The duplicity information was obtained from the Bright Star Catalogue (Hoffleit & Jaschek 1982; Hoffleit, Saladyga & Wlasuk 1983), Levato et al.(1987) and from preliminary findings by Verschueren et al.(1996) based on our data. A star is considered a radial velocity variable if it is listed as SB or SB1 in the Bright Star Catalogue or if Levato et al.or Verschueren et al.list it as a radial velocity variable. A star is considered a single-lined spectroscopic binary if the Bright Star Catalogue lists it as SBO or SB1O or if Levato et al.determined an orbit and list it as SB1. A star is considered a double-lined spectroscopic binary if any of these references list it as SB2 or SB2O. Note that the duplicity information pertains to duplicity that is apparent in the spectrum of the observed object; either through variability of the radial velocity or because of the presence of double lines. Thus, although some stars are part of a (wide) binary or multiple system, if there are no signs of duplicity in their spectrum they are listed as single stars. Finally, an asterisk after column

Table 3. Projected rotational velocities for early-type stars not related to Sco OB2.

HD	MK	$v \sin i$ km s ⁻¹	$\sigma(v \sin i)$ km s ⁻¹	Dupl.
28114	B6IV	27	4	
35039	B2IV-V	11	3	
36591	B1V	10	3	
45572	B9V	20	3	
57682	O9IV	24	5	
72660	A1V	7	2	
91316	B1Iab	66	6	SB1
179761	B8II-III	16	3	

(10) indicates that there is a note about that star in Appendix D. The notes contain information on the derivation of $v \sin i$. They also provide information about non-radial pulsations in the stars. These pulsations can have a sizeable effect on the line profiles and thus on the derived value of $v \sin i$. The information on the non-radially pulsating stars in our sample (including the β Cephei variables) was kindly provided by P. Groot.

For the star HD 140008 it was possible to measure $v \sin i$ for both components in the spectrum, and to within the error bars they both have the same $v \sin i$ of 11 km s⁻¹. Both components were taken into account in the subsequent analysis of the data. For method 2 the following stars were used as templates: HD 96706, HD 120709, HD 126341, HD 129056, HD 132955, HD 134687, HD 149438. In Table 3 we give the projected rotational velocities of the additional set of early-type stars that was observed with ECHELEC. Of these stars the following have been used as templates for method 2: HD 28114, HD 35039, HD 36591, HD 45572, HD 72660, HD 179761.

Finally, the stars HD 140008, HD 143118 and HD 144294 are listed as members of UCL by de Geus et al. (1989) but in order to be consistent with the subgroup boundaries as given by de Zeeuw et al. (1994) we list these stars as members of US.

3.5. Consistency of the Three Methods for Determining $v \sin i$

Figure 7 shows a comparison of the $v \sin i$ values derived using the three methods described above. In Fig. 7a the results from line-width measurements and template broadening are compared. All the values are consistent within the error bars. However, the values from line-width measurements are systematically lower, although generally this effect is $\lesssim 3$ km s⁻¹. This is an effect of the lowering of the apparent continuum due to rotational broadening. A lower continuum means that the measured line-widths are too small, which leads to underestimates of $v \sin i$.

Figure 7b shows the comparison of $v \sin i$ values derived from template broadening and fitting the He I $\lambda 4026$

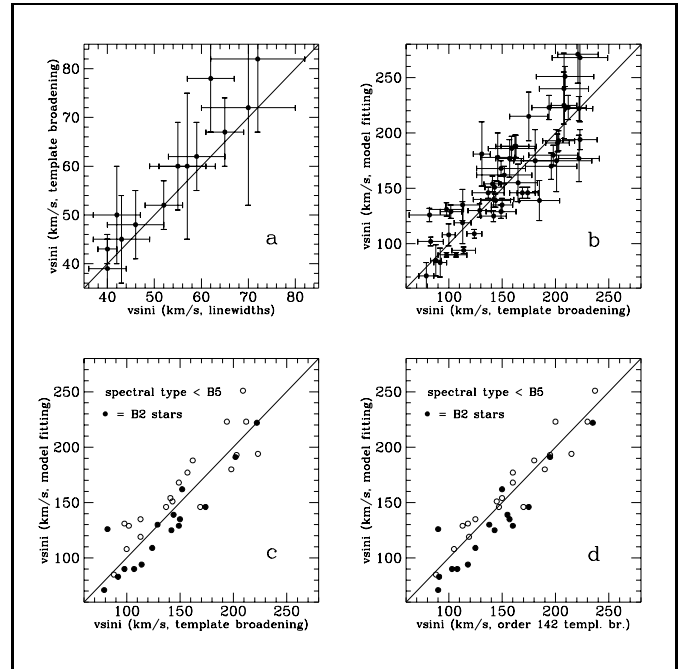


Fig. 7. Comparison of $v \sin i$ values obtained from measurements of line-widths, template broadening and fitting models to the He I $\lambda 4026$ line. Figure (a) shows the comparison between the line-width method and template broadening. Figure (b) shows a comparison of the results from template broadening and model fitting and (c) shows the same for stars of spectral type earlier than B5. The B2 stars are indicated as black dots. Figure (d) shows the same as (c) but now the template broadening values are derived from order 142 (containing the He I $\lambda 4026$ line) only. See the text for discussion.

line with models. Template broadening was applied for all spectral types over a large range of $v \sin i$. Thus, bearing in mind the discussion in Sect. 3.2 and Appendix C, we expect the two methods to yield inconsistent results for $v \sin i \gtrsim 150$ km s⁻¹. This can be clearly seen in Fig. 7b. For 17 out of the 52 stars in this figure the $v \sin i$ values from each method are inconsistent if one takes the error bars into account.

In order to understand Fig. 7b better we break the plot down according to spectral type. For spectral types earlier than B5 most stars have $v \sin i / v_{\text{br}} \lesssim 0.5$. The opposite is the case for later spectral types. So for later spectral types $w > 0.7$ (see Sect. 4 for a discussion on the relation between $v \sin i / v_{\text{br}}$ and w). That is precisely the range where template broadening fails. Figure 7c shows the comparison of the two methods if one leaves out spectral type B5 or later. The scatter at the high $v \sin i$ end is much reduced but overall it is still significant. We have also indicated the B2 stars separately and one can see that most of them have model fitting values that are lower. We noted in the previous section that this is to be expected if the B3 He I $\lambda 4026$ model lines are not strong enough compared to the data.

Figure 7d shows the comparison if one uses only the results for template broadening from order 142 (containing the He I $\lambda 4026$ line). Most of the B2 stars are displaced downwards, which is consistent with the remarks about B3 models made above. The other stars now lie closer to the line of consistent values and overall the scatter is somewhat reduced. The results in this figure suggest that the Balmer lines in other ECHELEC orders lead to underestimates of $v \sin i$ for template broadening. This is indeed confirmed if one compares the template broadening results of all other ECHELEC orders to those from order 142.

Another cause for inconsistencies between template broadening and model fitting comes from the fact that one has to make assumptions about the stellar parameters in model fitting. One needs to know the radius and mass of the stars in order to calculate v_{br} and hence $v \sin i$. This problem does not arise when one uses the classical model for rotational broadening. For example: CTC give a mass of $11 M_{\odot}$ and a radius of $5.8 R_{\odot}$ for a B1V star. However, according to the calibrations by Straižys & Kuriliene (1981) a B1V star has a mass of $12.9 M_{\odot}$ and a radius of $5.9 R_{\odot}$, while Schaller et al. (1992) use $9 M_{\odot}$ and $3.7 R_{\odot}$. These parameters lead to break-up-velocities of 491 , 527 and 556 km s^{-1} , respectively. So a variation of more than 10% in $v \sin i$ is possible due to uncertainties in stellar parameters.

We conclude that the three methods for obtaining $v \sin i$ are on the same velocity scale. However, caution should be exercised when comparing the results from template broadening to those of model fitting. The average difference between line-width and template broadening results is 7%, and for template broadening and model fitting this difference is 10%.

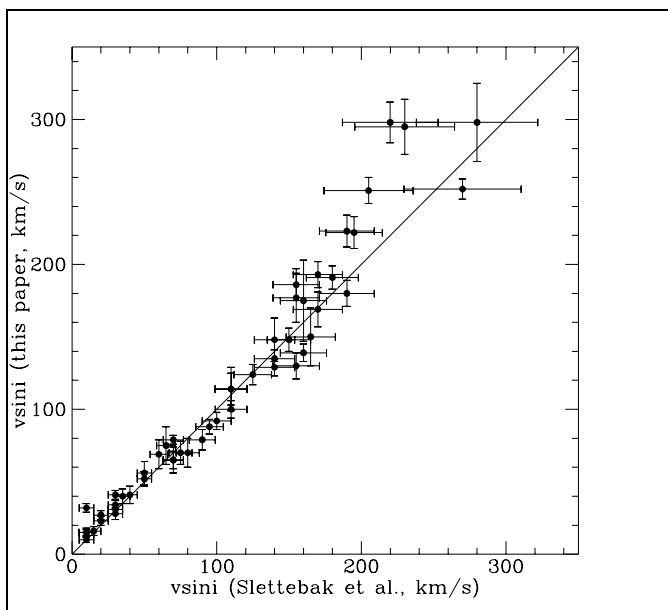


Fig. 8. Comparison of the $v \sin i$ values derived by SCBWP and the values derived in this paper.

3.6. A Comparison of $v \sin i$ Values for Standard Stars

We now turn to the comparison between our results and the values for $v \sin i$ listed for the standard stars in the system presented by Slettebak et al. (1975, hereafter SCBWP). They determined projected rotational velocities for stars with a range of spectral types and $v \sin i$. These measurements define a $v \sin i$ velocity scale to which other measurements can be compared.

Figure 8 shows the comparison between $v \sin i$ derived by us and the values listed in SCBWP (1975). We have 51 stars in our sample in common with SCBWP. The error bars on the values of SCBWP are assigned according to the accuracy given in their paper (10% for $v \sin i \lesssim 200 \text{ km s}^{-1}$ and 15% for $v \sin i \gtrsim 200 \text{ km s}^{-1}$), where for values of $v \sin i$ less than 50 km s^{-1} an error bar of 5 km s^{-1} is assigned. Within the error bars almost all $v \sin i$ values are consistent, but below about 60 km s^{-1} most of our values are systematically offset from those by SCBWP to higher $v \sin i$. The values of SCBWP are based on model calculations presented by Collins & Sonneborn (1977). They compared the equivalent width ratio of He I $\lambda 4471$ to Mg II $\lambda 4481$ to the model calculations to derive $v \sin i$. This procedure is not easy to compare to what we have done.

However, if we use the line-widths for Mg II $\lambda 4481$ as measured by SCBWP and calculate $v \sin i$ according to the modern models of CTC the discrepancies largely disappear and are no longer systematic. The new $v \sin i$ values were derived directly from the Mg II $\lambda 4481$ line-widths according to the procedure described in Collins & Truax (1995) after correction for the intrinsic and instrumental broadening of the line. Among the sharp-lined stars there are also two giants for which SCBWP used main-sequence models to derive $v \sin i$, which leads to underestimated values. Therefore, we conclude that our derived values of $v \sin i$ are on the same velocity scale as defined by SCBWP.

4. The Distribution of Rotational Velocities in Sco OB2

In this section we discuss the distribution of projected and true rotational velocities in Sco OB2. We concentrate on the known members of the association. Of the 156 stars we observed 88 are known members of the association (counting the double-lined spectroscopic binary HD 140008 as two objects). In order to increase the sample size we added $v \sin i$ values from literature for an additional 48 members (counting HD 145501 twice). The membership of these stars was taken from de Geus et al. (1989) and Bertiau (1958). The $v \sin i$ values were taken from Slettebak (1968) and Uesugi & Fukuda (1981). Their values are on the old velocity scale defined by the studies of Slettebak (1954, 1955, 1956, 1966a, 1966b, 1968) and Slettebak & Howard (1955), whereas our $v \sin i$ values are on the

velocity scale defined by SCBWP. In order to take the differences into account we corrected the literature values downwards by 15% and 5% for B-type stars and A-type stars, respectively, as recommended by SCBWP. In Table 4 we give the resulting values of $v \sin i$ for the literature sample. The columns have the same meaning as in Table 2. The stars HD 120908 and HD 138690 are members of UCL, all others are members of US. Note that HD 147889 is a doubtful member according to Bertiau (1958) and de Geus et al.(1989) do not list this star as a member. However, including or excluding this star from the analysis does not influence the results.

Table 5 shows the distribution among spectral type for the members of the subgroups of Sco OB2. The numbers in parentheses indicate the stars for which $v \sin i$ was obtained from literature. Note that the sample observed by us is very biased towards spectral types B0–B3 (see Sect. 2). If one assumes the initial mass function given in de Geus (1992) for Sco OB2, the numbers indicate that our observations are far from complete. Note also that of the 48 $v \sin i$ values from literature 46 are for stars in US and of these 33 are of spectral type B7–B9. All this means that caution should be exercised when comparing distributions of $v \sin i$ for the various subgroups.

4.1. The $v \sin i$ Distributions in the Sco OB2 Subgroups and the Binary Population

Figures 9 and 10 show the distributions of $v \sin i$ and $v \sin i / v_{\text{br}}$ for Sco OB2 and each of the subgroups for which membership studies have been done. In both figures we indicate the distributions of single stars and binaries (spectroscopic binaries and radial velocity variables) separately, with solid and dotted lines respectively. Both figures suggest that amongst the binaries there is a higher proportion of slow rotators. We tested this by performing a robust-rank-order test on the members of Sco OB2 that we have observed and for which we have good information on duplicity (see Table 2). This is a non-parametric statistical test that is designed to test for differences in the median of two samples (see e.g., Siegel & Castellan 1988). Nothing is assumed a priori about the underlying distributions. For the $v \sin i$ distributions this test confirms at a confidence level of more than 99.99% that the single stars have a higher median $v \sin i$. For the $v \sin i / v_{\text{br}}$ distributions the same result is obtained. This implies that the bulk of the single stars has a higher projected rotational velocity. We find the same result if we use all the members of Sco OB2 (assuming that stars for which we have no duplicity information are single).

The finding that binaries show lower rotational velocities can be interpreted as a consequence of the deposition of part of the total angular momentum in the orbit of the system at formation or as a consequence of tidal braking in very close binaries. Levato et al.(1987) have shown, using the $v \sin i$ data of Slettebak (1968), that there is a corre-

lation between the frequency of duplicity and the average $v \sin i$ for the subgroups US and UCL. This correlation is in the sense that stars in UCL rotate slower on average and that the frequency of duplicity is higher in that subgroup. Based on the duplicity data in Tables 2 and 4 we also find a higher proportion of binaries in UCL than in US. However the distributions of rotational velocities are not significantly different for these two subgroups.

If one looks at the data in more detail it turns out that most of the single stars at high $v \sin i$ values are stars added from the literature in the spectral type range B7–B9, whereas our sample contains mainly B0–B6 stars (see Sect. 2). Most of the literature data (46 out of 48 stars) was added to US and indeed the difference between the single and binary stars is most pronounced for this subgroup (see Figs. 9 and 10). In US the extra literature data consist of 28 stars for which $v \sin i \geq 150 \text{ km s}^{-1}$. Of these stars 15 are single stars in the B7–B9 range. The sample observed by us contains, in contrast, only one single B7–B9 star in the same $v \sin i$ range. To check whether the stars in the B7–B9 range rotate faster we divided the sample in B0–B6 and B7–B9 single stars. Each of these samples was then divided into stars for which $v \sin i \geq 150 \text{ km s}^{-1}$ and $v \sin i < 150 \text{ km s}^{-1}$. Subsequently, a 2×2 contingency table analysis was done on the data with the Fisher exact probability test (see e.g., Siegel & Castellan 1988). The test confirms at a confidence level of more than 99.99% that the B7–B9 single star sample contains more objects with $v \sin i \geq 150 \text{ km s}^{-1}$. If one does the same test for $v \sin i / v_{\text{br}}$ with the division of the samples at 0.4 then the same result is found at the 99.98% confidence level. The value 0.4 follows from the fact the all B7–B9 stars with $v \sin i \geq 150 \text{ km s}^{-1}$ have $v \sin i / v_{\text{br}} \geq 0.4$. Thus, it could be that late B-stars exhibit intrinsically faster rotation. However, this finding is based on inhomogeneous $v \sin i$ data. To really interpret the $v \sin i$ data, a more complete coverage of the spectral types is needed in all subgroups of Sco OB2 and a complete census of the binary population as a function of spectral type is also required.

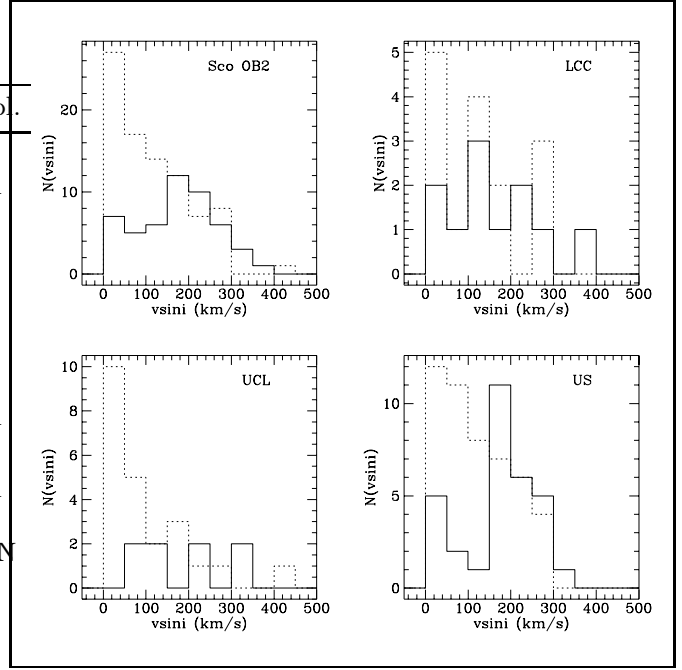
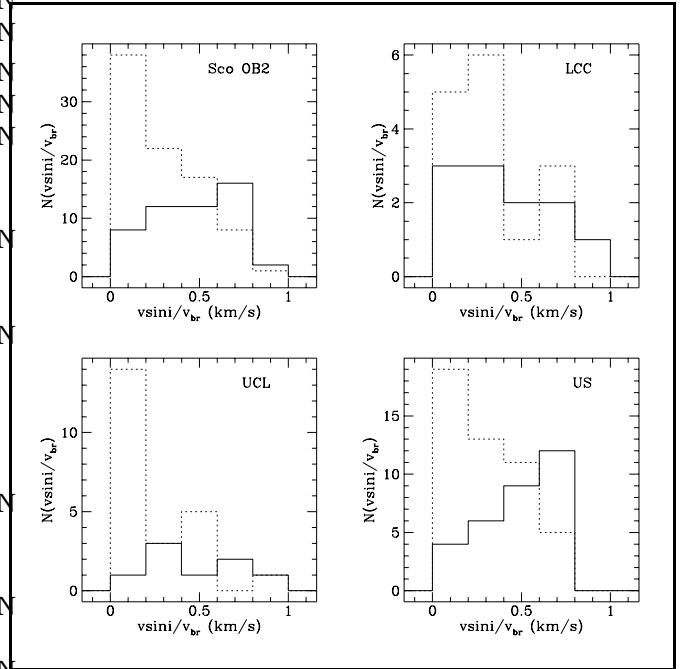
Finally, we remark that there are no significant differences between the subgroups of Sco OB2 for the median value and the overall distribution of $v \sin i$ or $v \sin i / v_{\text{br}}$.

4.2. Tests of Various Hypotheses about the Distribution of Intrinsic Rotational Velocities

We now test various hypotheses about the distribution of intrinsic rotational velocities against the data. We wish to investigate whether any constraints can be placed on the distributions of true rotational velocities and/or the orientation of rotation axes. This will lead to constraints on the origin of angular momentum in stars and on the star formation process. So far the only models for $v \sin i$ distributions that provide detailed predictions are the ones that assume a random selection process. The magnitude of the rotational velocity and the inclination angle of the rota-

Table 4. Projected rotational velocities for the literature sample.

HD	MK	$v \sin i$	v_{br}	$\frac{v \sin i}{v_{br}}$	Mem.	Dup.
120908	B5III	85	308	0.276	M	
138690	B2IV	229	412	0.557	M	SB1
138485	B2Vn	212	459	0.463	M	RV
138764	B6IV	17	342	0.050	M	RV
139094	B8IV/V	153	363	0.421	M	
139486	B9V	212	350	0.607	M	RV
141404	B9.5IV	170	350	0.486	M	
141774	B9V	136	350	0.389	M	RV
142165	B5V	204	388	0.526	M	SB1
142250	B7V	42	373	0.114	M	RV
142315	B9V	255	350	0.729	M	SB1
142378	B2/B3V	204	411	0.496	M	RV
142884	B8/B9III	170	283	0.601	m	CON
143567	B9V	153	350	0.437	M	RV
143600	B9.5V	255	350	0.729	M	RV
143699	B6III/IV	144	303	0.477	M	RV
144334	B8V	38	363	0.105	M	
144661	B8IV/V	85	363	0.234	M	RV
145102	B9VpSi	34	350	0.097	M	RV
145353	B9V	187	350	0.534	M	
145501(1)	B8V+B9VpSi	59	357	0.167	m	RV
145501(2)	B8V+B9VpSi	63	357	0.179	m	RV
145519	B9Vn	255	350	0.729	M	SB1
145554	B9V	153	350	0.437	M	CON
145631	B9V	153	350	0.437	M	CON
145792	B6IV	21	342	0.062	M	CON
146001	B8V	170	363	0.468	M	CON
146029	B9V	212	350	0.607	M	CON
146284	B9III/IV	170	278	0.612	M	
146285	B8V	136	363	0.375	M	RV
146416	B9V	255	350	0.729	M	CON
146706	B9V	229	350	0.656	m	
146998	A2pSr	23	350	0.068	m	
147009	B9.5V	136	350	0.389	M	CON
147010	B9II/III	21	278	0.076	m	RV
147196	B6/B7Vn	297	377	0.789	M	
147701	B5III	68	308	0.221	m	
147703	B9Vn	238	350	0.680	m	
147888	B3/B4V	153	406	0.377	M	CON
147889	B2III/IV	85	364	0.234	M	RV
147890	B9.5pSi	25	350	0.073	M	RV
147932	B5V	153	388	0.394	m	CON
147955	B9V	238	350	0.680	m	
148199	B9VSi	17	350	0.049	m	CON
148579	B9V	127	350	0.364	M	RV
148594	B8Vnn	255	363	0.702	M	CON
148605	B2V	195	459	0.426	M	CON
148860	B9.5V	255	350	0.729	m	

**Fig. 9.** The distribution of $v \sin i$ values for the members of Sco OB2. The distribution for the whole association is shown as well as for each subgroup separately. The solid lines show the distribution for the single stars and the dotted lines show the distribution for the binaries (radial velocity variables and known spectroscopic binaries).**Fig. 10.** Same as Fig. 9 for the distribution of $v \sin i / v_{br}$.

tion axis are selected separately and randomly according to a certain prescription. These models do not take into account the physically more likely possibility that a star

Table 5. Distribution of spectral types for the members of Sco OB2.

Subgroup	O	B0–B3	B4–B6	B7–B9	A
US	1	25 (5)	3 (7)	3 (33)	1 (1)
UCL	0	18 (1)	6 (1)	5	0
LCC	0	18	6	2	0

is formed with a certain angular momentum. The role of stellar mass and the star formation process is also ignored.

We assume in all cases that the rotation axes are oriented randomly in space. This means that the distribution of inclination angles i is given by:

$$f(i) di = \sin i di. \quad (1)$$

In what follows we define v_e to be the true equatorial rotational velocity of the star, $\eta = v_e/v_{\text{br}}$ and $y = v \sin i/v_{\text{br}}$. Again, v_{br} is the true equatorial velocity of the star at break-up, and w is the fraction of the corresponding critical angular velocity. Note that in case the Roche model is assumed for the rotating star, $v \sin i$ is not equal to $v_{\text{br}} \times w \times \sin i$ and that it makes a difference whether η or w is chosen randomly to generate the distribution of y . In the Roche model the star rotates uniformly and its surface follows an equipotential surface. The potential is generated by a point mass at the centre of the star. The equation describing the surface is:

$$\Phi = \frac{GM}{R} + \frac{1}{2}\omega^2 R^2 \sin^2 \theta = \frac{GM}{R_p}. \quad (2)$$

Φ is the total potential consisting of a gravitational and a centrifugal term. The mass of the star is M and the distance from the surface to the centre is given by R . The polar radius is R_p , which remains constant, and θ is the latitude on the surface of the star as measured from the pole. The critical angular velocity follows by setting $\mathbf{g} = -\nabla\Phi = 0$ and is given by: $\omega_c^2 = 8GM/27R_p^3$. With $w = \omega/\omega_c$ and setting $x = R/R_p$ Eq. (2) becomes:

$$\frac{1}{x} + \frac{4}{27}w^2 x^2 \sin^2 \theta = 1. \quad (3)$$

Now, from the definitions of ω_c , x and w it follows that $\eta = \frac{2}{3}wx$, where x is to be evaluated at the equator. This value of x follows by setting $\theta = \pi/2$ in Eq. (3) and solving this equation for x for a given w . The equation can be solved analytically and it follows that:

$$\eta = -2 \cos\left(\frac{\arccos w - 2\pi}{3}\right). \quad (4)$$

It is this transformation between w and η that one has to take into account if the distribution of y is generated by picking w randomly.

We tested the following models for the distribution of intrinsic rotational velocities of the stars:

1. The value of w is distributed homogeneously on $[0, 1]$.
2. The value of η is distributed homogeneously on $[0, 1]$.
3. The distribution of v_e is given by a Maxwellian.
4. The distribution of w is given by a truncated Maxwellian. ■

All the hypotheses about the distribution of v_e are variations on the assumption of a completely random distribution of rotational velocities. So the question is whether one can exclude any form of total randomness in the v_e or w distribution. If all these models are excluded by the data then either one has to relax the assumption of random orientation of rotation axes or a non-random process for generating the distribution of rotational velocities has to be assumed. We find no correlation in our data between $v \sin i$ and Galactic longitude, which is consistent with the assumption of random orientation of rotation axes.

For the four models above one can derive an expression for the distribution of y by using the formula given by Chandrasekhar & Münch (1950):

$$\phi(v \sin i) = v \sin i \int_{v \sin i}^{\infty} \frac{f(v_e)}{v_e \sqrt{v_e^2 - (v \sin i)^2}} dv_e, \quad (5)$$

where $\phi(v \sin i)$ is the distribution function of $v \sin i$ and $f(v_e)$ that of v_e . If there is a break-up velocity, then Eq. (5) becomes (in terms of y and η):

$$\phi(y) = y \int_y^1 \frac{f(\eta)}{\eta \sqrt{\eta^2 - y^2}} d\eta, \quad (6)$$

The form of $\phi(y)$ for model 2 is derived in Chandrasekhar & Münch (1950, their Eq. (26)). To derive $\phi(y)$ for model 1 one should use

$$f(\eta) = f(w) \left| \frac{dw}{d\eta} \right|, \quad (7)$$

with:

$$\left| \frac{dw}{d\eta} \right| = \frac{3}{2}(1 - \eta^2). \quad (8)$$

Deutsch (1970) showed, using arguments from statistical mechanics, that if ω is distributed isotropically with mutually independent Cartesian components the distribution of ω is given by a Maxwellian. The form of the distribution function is:

$$f(z) = \frac{4}{\sqrt{\pi}} z^2 e^{-z^2}, \quad (9)$$

where $z = j\omega$ and j is a parameter with the dimensions ω^{-1} . It follows that the distribution of $v \sin i$ is then given by:

$$\phi(u) = 2ue^{-u^2}, \quad (10)$$

where u is $jv \sin i$ and $1/j$ is the root mean square value of $v \sin i$ which is the same as the modal value of v_e for a Maxwellian (see Deutsch 1970). This is the distribution of $v \sin i$ for model 3. Note that it is assumed that there is no

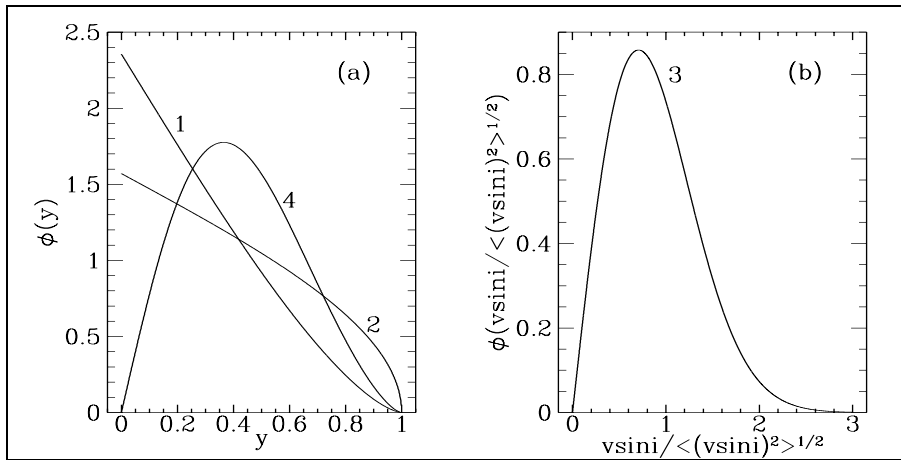


Fig. 11. (a) The distribution functions of $y = v\sin i/v_{\text{br}}$ for models 1, 2 and 4. (b) The distribution function of $v\sin i$ for model 3. The models are indicated by their corresponding numbers.

break-up velocity in this case. To derive the distribution for model 4 one should take into account that $\omega \leq \omega_c$. We chose to model this simply by truncating the Maxwellian at ω_c and normalizing the resulting distribution. In terms of η one can find $\phi(y)$ by using Eqs. (4), (6) and (7). The distribution of w is now given by:

$$f(w) = \frac{\frac{4}{\sqrt{\pi}} w^2 e^{-w^2}}{\text{erf}(1) - \frac{2}{\sqrt{\pi}} e^{-1}}, \quad (11)$$

where erf is the error function.

The distribution functions for y for models 1, 2 and 4 are listed in Table 6 (model 3 being given by Eq. (10)). For model 4 the integral in Eq. (6) has to be evaluated numerically. All the $\phi(y)$ are shown in Fig. 11. Note that models 3 and 4 show a peak in the distribution at intermediate values of $v\sin i$ and $v\sin i/v_{\text{br}}$ whereas models 1 and 2 predict a large number of slow rotators.

Table 6. Distribution functions for $y = v\sin i/v_{\text{br}}$.

Model	$f(\eta)$	$\phi(y)$
1	$\frac{3}{2}(1 - \eta^2)$	$-\frac{3}{2}y\sqrt{1 - y^2} + \frac{3}{2}\arccos y$
2	1	$\arccos y$
4	$\frac{3}{2}(1 - \eta^2) \frac{\frac{4}{\sqrt{\pi}} w^2 e^{-w^2}}{\text{erf}(1) - \frac{2}{\sqrt{\pi}} e^{-1}};$ $w = \cos(\arccos(\frac{-\eta}{2}))$	$y \int_y^1 \frac{f(\eta)}{\eta\sqrt{\eta^2 - y^2}} d\eta$

The models were compared to the data by calculating the Kolmogorov-Smirnoff statistic D and the probability P that D exceeds the observed value under the hypothesis that the data were drawn from the model distribution (see

e.g., Press et al.1992). A model was rejected if $P < 0.05$. As argued in the previous section, the B7–B9 stars may be a group of stars that rotate intrinsically faster than B0–B6 stars. Our data consist primarily of B0–B6 stars and adding literature data on later types only to US may introduce artifacts in the $v\sin i$ distribution that are the result of our sample selection. Thus we decided to compare the model distributions only to the B0–B6 stars.

We did the KS-test for Sco OB2 as a whole and for each subgroup. The data were also divided in single stars and binaries. The binaries include the spectroscopic binaries as well as the radial velocity variables. The comparison of the models to the data was focused on the members of Sco OB2. We are interested here in the distribution of rotational velocities in a group of physically related stars. The results are shown in Table 7. In this table a “+” indicates that the model was not rejected and a “–” indicates that the model was rejected.

The number of measurements for each subgroup is rather small (40 stars in US, 26 in UCL and 24 in LCC), which makes it difficult to distinguish between models. The data for the single stars are compatible with all models. This is probably the result of the limited amount of data. If we take only the data for US into account and include the B7–B9 stars we find that only model 4 is consistent with the data. It is not warranted, however, to conclude that the formation of single stars leads to an isotropic distribution of angular momentum vectors. We have shown in the previous section that the B7–B9 stars rotate faster than B0–B6 stars. So there is an effect with stellar mass that model 4 does not take into account.

For the binary stars it seems that only model 1 is consistent with the data. What does it mean if we assume that this model actually describes the data? Do components of binary stars acquire a random fraction of their critical angular velocity or is model 1 the only model that predicts enough slow rotators? Remember that binary components show intrinsically slower rotation than the single stars. This may be due to the redistribution of angular momentum into orbital angular momentum.

Table 7. Results of comparing model distributions to the data (B0–B6 members). A “-” indicates that the model is rejected. A “+” indicates that the model is not rejected. The number of stars in each data set is indicated in parentheses.

Model	Sco OB2			US		
	All (90)	Single (23)	Binary (67)	All (40)	Single (9)	Binary (31)
1	+	+	+	+	+	+
2	-	+	-	+	+	-
3	-	+	-	+	+	+
4	-	+	-	-	+	-

Model	UCL			LCC		
	All (26)	Single (5)	Binary (21)	All (24)	Single (9)	Binary (15)
1	+	+	+	+	+	+
2	-	+	-	+	+	+
3	-	+	-	+	+	+
4	-	+	-	-	+	+

If one aims at putting real constraints on the star formation process by looking at the distribution of rotational velocities, then models are needed that take into account the details of this process. How does the combination of stellar mass, angular momentum and interior structure translate into an observed rotational velocity? So far no detailed predictions of this kind have been made. Mouschovias (1983) does give an estimate of the equatorial velocity of the star as it arrives on the zero-age main-sequence. His prediction follows from a consideration of magnetic braking in the early stages of star formation. As soon as the protostellar condensation is dense enough to decouple from the surrounding magnetic field its angular momentum is basically determined. It then follows that:

$$v_e \propto \rho^{2/3} R M_C, \quad (12)$$

where R and ρ are the mean density and radius of the protostar and M_C is the mass of the cloud-core from which the protostar formed. The factor $\rho^{2/3} R$ increases going from O to F0 stars. If one assumes that the mass of the cloud-core scales with the mass of the star that forms from it, this equation predicts a maximum in the rotational velocities somewhere between O and F stars. This is consistent with the observed distribution of velocities for field stars (e.g., Wolff et al. 1982), and with our observed distribution of rotational velocities as a function of spectral type.

Another model for the origin of angular momentum in stars that takes the star formation process into account is given by Wolff et al. (1982). They find a large number of slow rotators in their data that cannot be explained by the presence of binaries. Therefore they propose that all protostars start out in a state of low angular momentum. Subsequently, a number of them acquire higher angular mo-

menta through gravitational interactions with other protostars or protostellar condensations in a forming cluster. This model then predicts a concentration of rapid rotators in the centres of clusters and associations. We cannot see this clearly in our data and in our case the presence of binaries can account for the excess of slow rotators with respect to a Maxwellian.

To go further more detailed predictions of the distribution of rotational velocities are needed that take the star formation process into account. Observationally, more data are required ($v \sin i$ as well as duplicity information) for the members of Sco OB2 of spectral types later than B6. This will facilitate a study of $v \sin i$ as a function of mass and of the relation to duplicity.

5. Rectifying the $v \sin i$ Distribution

In the previous section we compared model v_e and v_e/v_{br} distributions to the observed $v \sin i$ distribution in Sco OB2. In this section we present the distributions of v_e and v_e/v_{br} that follow directly from the rectification of the observed $v \sin i$ distribution under the (sole) assumption of randomly oriented rotation axes. Two techniques are used to do so; Lucy-iteration (Lucy, 1974) and the technique presented by Bernacca (1970).

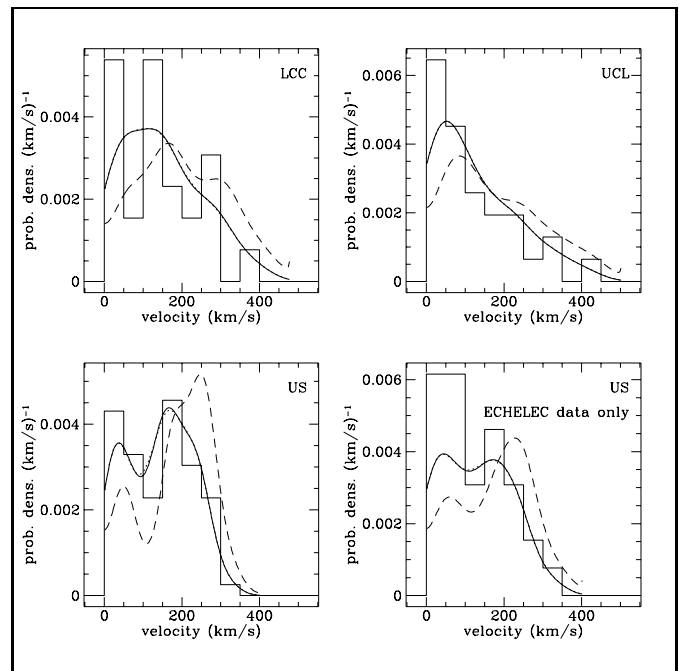


Fig. 12. Results of applying the Lucy iterative technique for the rectification of $v \sin i$ distributions. The number of iterations used was 8, 9, 11 and 9 for LCC, UCL, US and the ECHOLEC data in US, respectively. The data histograms are shown for comparison. The solid lines indicate $\hat{\varphi}(v \sin i)$, the dashed lines are for $\psi(v_e)$ and the short-dashed lines are for $\varphi(v \sin i)$.

For both techniques it is necessary to have a good estimate of the observed probability density function (PDF). We used a so-called kernel estimator. The PDF is represented as a sum of kernel functions, each corresponding to a single data point. The kernel function is normalized to unity and it is characterized by a width h . The width depends on the observed distribution of the data. A rule of thumb for calculating h is given in Vio et al. (1994). The kernel estimator provides a smooth estimate of the PDF. We used Gaussian kernels, in which case h corresponds to the standard deviation.

For both rectification techniques the interval for the kernel-estimate of the PDF was restricted to $v \sin i \geq 0 \text{ km s}^{-1}$. For the Lucy-iteration the upper limit of the interval was set by increasing the data interval in small steps until the cumulative distribution increased by no more than 0.01%. In the technique given by Bernacca (1970) one assumes that there is an upper limit to $v \sin i$. We used the break-up velocity of the stars as a function of spectral type and rectified the $v \sin i / v_{\text{br}}$ distribution. So the PDF was restricted between 0 and 1. In both cases the kernel-estimator formally has tails outside the intervals mentioned above, and we decided to simply re-normalize the PDF on the restricted intervals.

For the iterative technique given by Lucy (1974) we used the optimum stopping criterion described in Lucy (1994). In his paper two quantities are defined:

$$H = \sum_{i=1}^N \tilde{\varphi}_i \ln \varphi_i \quad (13)$$

and

$$S = - \sum_{i=1}^N \psi_i \ln \psi_i, \quad (14)$$

where H is $N^{-1} \times$ the log-likelihood of the data vector $\tilde{\varphi}$ (this vector being the estimate of the PDF described above), with φ the data vector that one derives from the rectified distribution ψ . S is a function that decreases as the solution ψ increases in complexity (Note that we took χ_j constant in Eq. (6) of Lucy 1994). The solution ψ will describe a trajectory in the (H, S) plane during iteration and one can define the curvature of this trajectory as:

$$\kappa = \frac{|S\ddot{H} - H\ddot{S}|}{(S^2 - H^2)}. \quad (15)$$

It turns out that the iterations should be stopped when κ passes through a minimum.

Figure 12 shows the results of rectifying the observed $v \sin i$ distributions for the members of each subgroup of Sco OB2. For US we also show the result of rectification if we use only our own data. In all figures the data histogram is shown. The solid line is the estimate of the observed PDF $\tilde{\varphi}(v \sin i)$, the dashed lined is the rectified distribution

$\psi(v_e)$ and the short-dashed line is the PDF $\varphi(v \sin i)$ that follows from ψ .

Figure 12 suggests that the peak in the v_e distribution lies at increasingly higher values going from UCL to LCC to US. This result is the same even if only our own data for US are used. Whether this effect is due to a decrease in binary frequency per subgroup is hard to tell. The data are incomplete for the B7–B9 stars for UCL and LCC. If one takes only B0–B6 stars into account and only our sample the binary frequency increases from LCC to UCL to US, opposite to the expected trend. However if one takes all the data into account then the binary frequency increases from LCC to US to UCL. We stress here again that the differences between the subgroups are not statistically significant. An improved sample is needed to settle this issue.

It is interesting that the shift in the peak of the v_e distribution correlates with the ages of the subgroups. This suggests that the shift could also be due to evolutionary effects. Stars that evolve off the main sequence expand their outer layer and this may lead to a lowering of v_e . This effect should be most pronounced in the giants and supergiants. The percentage of stars in these luminosity classes is, however, very similar for the three subgroups. If one also takes sub-giants into account then indeed UCL has the highest percentage of evolved stars, but the difference with the other subgroups is small. Moreover UCL and US have similar percentages of evolved stars. Apart from the statistics, the magnitude of evolutionary effects depends much on whether or not stars rotate differentially.

A drawback of the Lucy-rectification results presented above is that the existence of a break-up velocity is not taken into account. Yet, the $v \sin i$ values we derived for rapid rotators are based on the value of the break-up velocity for the star in question. The rectification technique presented by Bernacca (1970) does take the existence of an upper limit on v_e into account. If there is a break-up velocity then one can define an angle θ by:

$$v \sin i = v_{\text{br}} \sin \theta. \quad (16)$$

It is clear that the inclination angle i must then satisfy $\theta \leq i \leq \pi/2$. So one has more information about the rotation axes of the stars. If one assumes that the rotation axes are randomly distributed in space with the restriction on i given above, the distribution of i , $f(i)$, can be derived from the observed $v \sin i$ distribution:

$$f(i) = \sin i \int_0^{\sin i} \frac{\phi(y)}{\sqrt{1-y^2}} dy. \quad (17)$$

The distribution of v_e/v_{br} (η) is then given by:

$$f(\eta) = \frac{1}{\eta^2} \int_0^\eta \frac{y^2 \phi(y)}{\sqrt{\eta^2 - y^2} \sqrt{1 - y^2}} dy. \quad (18)$$

For a derivation see Bernacca (1970). We have translated his formulas to y and η .

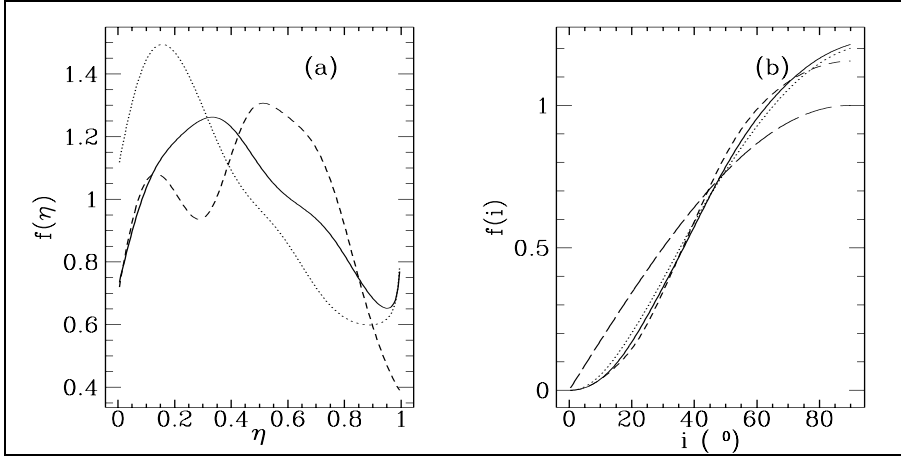


Fig. 13. (a) shows the distributions of $\eta = v_e/v_{br}$ for the subgroups of Sco OB2 derived with the technique of Bernacca (1970). The solid line indicates the result for LCC, the short-dashed line that for UCL and the dashed line indicates the result for US. The upturns in the distributions for LCC and UCL at $\eta = 1$ are probably not real but due to the singularity in the integral in Eq. (18). (b) shows the corresponding distributions of i . In this figure the long-dashed line indicates the distribution $f(i) = \sin i$.

Thus, with the technique of Bernacca one can derive the distribution of i as well as η and the distribution of η is now given by an integral which can be evaluated numerically. The results for the three subgroups of Sco OB2 are shown in Fig. 13. We used the same estimates of the observed PDF as for the Lucy-rectification as input for Eq. (18). The resulting distributions of η (Fig. 13a) show the same trend as the v_e distributions in Fig. 12. Namely, a shift of the peak towards higher values of η going from UCL to LCC to US. Note that the up-turns in the distributions for LCC and UCL at $\eta = 1$ are probably not real but due to the singularity in the integral in Eq. (18). The distributions of i (Fig. 13b) are all very similar and essentially the difference from the distribution given in Eq. (1) is that there are less stars seen pole-on and more seen equator-on.

6. Effects of Rotation in the Hertzsprung-Russell Diagram

Rapidly rotating stars have deformed surface layers and their surface gravity varies from the pole to the equator. The atmospheric zones around the pole have close to normal surface gravities and thus emit an almost normal stellar spectrum. The zones close to the equator, however, have lower surface gravities and also suffer from obscuration due to gravity darkening. The stellar spectrum emitted from these zones then corresponds to lower surface gravities as well as lower effective temperatures. This implies that one expects changes in the photometric colours of the stars with rotation. These changes are a function of the inclination angle as well as the rotation speed.

These effects have been calculated by a number of authors for various photometric systems (see e.g., CTC and references in Tassoul, 1978). In general stars are displaced away from the main-sequence and the main-sequence for rotating stars always appears brighter than its non-rotating counterpart. Stars observed pole-on are displaced vertically towards higher luminosities and stars

seen equator-on are displaced more along the main sequence towards lower T_{eff} .

The effects of rotation on the Walraven photometric system have not been studied previously. In this section we investigate whether there are stars for which the Walraven colours indeed correlate with $v \sin i$. We investigate unevolved members of the Sco OB2 association in order to avoid the effects of stellar evolution on the colours. The oldest subgroup in Sco OB2 has an age of 14–15 Myr and this implies that the upper mass limit for stars still on the main sequence is about $12 M_\odot$ (using the models by Schaller et al. 1992). This mass corresponds to stars of spectral type $\sim B1$ (see e.g., Harmanec 1988). In the following we concentrate on the B1–B9 stars to find out whether there are effects of rotation on Walraven colours.

For the stars in our data we used the Walraven photometry of de Geus et al. (1990) and the value of $\log T_{\text{eff}}$ and $\log g$ was taken from de Geus et al. (1989). For some stars we had to derive $\log T_{\text{eff}}$ and $\log g$ from the photometry and that was done as described in de Geus et al. (1989) and Brown et al. (1994). In Fig. 14a we show the HR-diagram in the $\log g$ – $\log T_{\text{eff}}$ plane for all B1–B9 main sequence dwarfs that are members of Sco OB2. Binaries were excluded from this diagram as well as B9p stars. The latter are known to have peculiar spectra and rotate slowly as a class. In Fig. 14a the symbol size scales with $v \sin i / v_{br}$. It is clear that for $\log T_{\text{eff}} < 4.2$ the stars with large values of $v \sin i / v_{br}$ lie above the main sequence. In this temperature range one finds B7–B9 stars. The Kelvin-Helmholtz time-scale for these stars is $\sim 2\text{--}5 \times 10^5$ yr. Even for members of US this is short enough for all B7–B9 stars to have evolved onto the zero-age main-sequence. Thus we do not expect any pre-main-sequence stars among this group.

The only other reason for these stars to lie above the main sequence is that the transformation of the photometry to $\log T_{\text{eff}}$ and $\log g$ is in error. We therefore show the same sample of stars in the Walraven $[B - U]$ vs. $[B - L]$ diagram in Fig. 14b. The ZAMS is drawn in and the early type B-stars ($[B - L] < 0.05$) all lie on or very near this isochrone. In this colour-colour diagram the evolution of

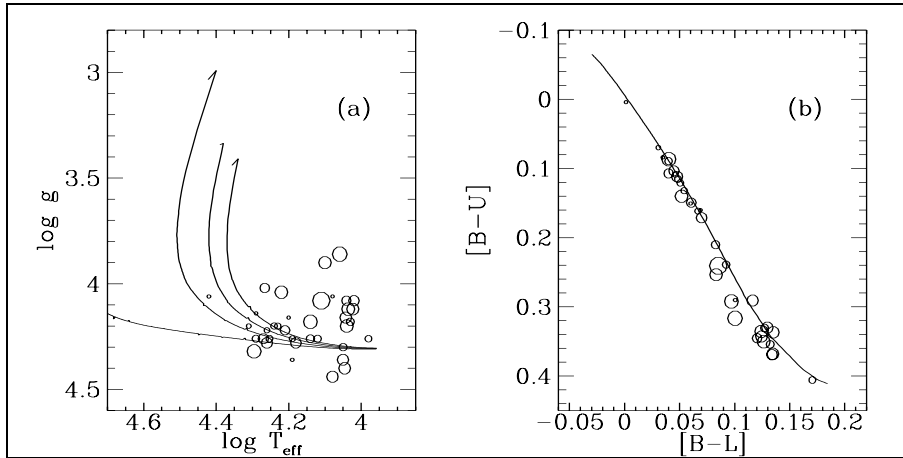


Fig. 14. (a) The Hertzsprung-Russell diagram in $\log T_{\text{eff}}$ and $\log g$ for B1–B9 dwarfs that are members of Sco OB2 (b) The Walraven $[B-U]$ vs. $[B-L]$ colour-colour diagram. In both figures only single stars are included and the B9p stars are excluded. The symbol size scales with $v \sin i / v_{\text{br}}$ and isochrones (from Schaller et al.1992) are shown for 0, 5, 10 and 15 Myr in (a) and for 0 Myr in (b).

a star away from the ZAMS is towards the lower left (see de Geus et al.1989). It is clear that for $[B-L] > 0.05$ the stars are displaced away from the ZAMS in the direction where evolved stars are expected. If we calculate the distance of each B7–B9 dwarf from the ZAMS (defined as the distance to the nearest point on the isochrone) and correlate that distance with $v \sin i / v_{\text{br}}$, we find a correlation at the 95.2% confidence level. Thus the photometry is indeed affected by rotation for the B7–B9 stars.

The largest decrease in $\log g$ in Fig. 14a is 0.44 for a star with $v \sin i / v_{\text{br}} = 0.84$. The latter value implies that $w \geq 0.96$. Judging from Fig. 2 in Collins (1963) the value of the surface gravity then varies over a factor of ~ 3 from pole to equator. This is consistent with our observed factor of 2.8. We conclude that the Walraven colours are affected by stellar rotation.

Note that some stars in Fig. 14b are located just above the ZAMS. It concerns a B2V, two B4V, a B8V and two B9V stars. One of the B4V stars is a star with emission lines. There is nothing peculiar about the other stars. The positions of the normal B2V and B4V stars can be explained as observational errors. The B8 and B9 stars however, lie further away from the ZAMS than the errors allow. This can be explained by the fact that for B7–B9 stars the empirical ZAMS for the Walraven system, as given in Brand & Wouterloot (1988), lies just above the ZAMS defined by Schaller et al.(1992).

The lower surface gravity derived for the B7–B9 stars affects age determinations based on isochrone fitting as well as the derivation of mass distributions. The age of subgroups in the association will appear higher because of the apparent presence of evolved B7–B9 stars. However, we note that the ages derived by de Geus et al.(1989) are not affected by rotation. The stars in the B7–B9 range had little weight in the isochrone fitting procedure. The same holds for the ages derived for the Ori OB1 subgroups by Brown et al.(1994), who excluded the B7–B9 stars from their isochrone fitting procedure. The IMFs derived by de Geus (1992) and Brown et al.(1994) for Sco OB2 and Ori OB1, respectively, are not affected by rotation. In both

cases the mass range used by the authors excluded B7–B9 stars.

7. Conclusions and Future Work

We have presented $v \sin i$ values for 156 established or probable members of the Sco OB2 association. The projected rotational velocities were derived from echelle spectra using three different techniques, depending on the anticipated value of $v \sin i$. We have shown that the results for the different techniques are consistent and that our results are consistent with the standard system of SCBWP. On average the errors on our $v \sin i$ values are $\sim 10\%$.

We analyzed our own data together with data for members of Sco OB2 taken from the literature. The analysis of the $v \sin i$ distributions for the members of Sco OB2 reveals that there are no significant differences between the subgroups in Sco OB2. The binary stars in Sco OB2 rotate slower on the whole than the single stars. This is consistent with a picture in which angular momentum is transferred to the binary orbit during star formation, and possibly further removed due to tidal braking. For US we showed that the B7–B9 single stars rotate significantly faster than the B0–B6 stars. This may be consistent with the prediction about the distribution of rotational velocities given by Mouschovias (1983). However, this result is derived from inhomogeneous data.

Given the present data we cannot definitely exclude a form of random distribution of intrinsic rotational velocities. The number of single stars in the data is not enough to get statistically significant results. Inclusion of the binaries complicates the picture due to the different physical mechanism by which binary components may acquire a low rotational velocity.

The rectification of the $v \sin i$ distributions by either the technique of Lucy (1974, 1994) or that of Bernacca (1970), suggests that the peak in the distribution of rotational velocities shifts to higher values going from UCL to LCC to US. The interpretation of this finding in terms of

binary fraction per subgroup or evolutionary effects is not possible with the present data.

For the Walraven photometric system we have now for the first time shown conclusively that the colours of stars are affected by rotation. This is most notably the case for the B7–B9 stars, where the distance to the ZAMS in the $[B-U]$ vs. $[B-L]$ diagram correlates with $v \sin i$. However, we also conclude that the determination of ages and mass distributions for Sco OB2 (de Geus et al.1989, de Geus 1992) and Ori OB1 (Brown et al.1994) are not affected by rotation.

The first step in improving the analysis of the $v \sin i$ distributions in Sco OB2 is to get a complete sample in all subgroups. This entails selecting members on the basis of kinematic data and performing a complete census of the binary population. It is very timely that the data from the HIPPARCOS astrometric mission will become available in early 1996. The SPECTER consortium in Leiden (see de Zeeuw et al.1994) was granted observing time on this mission and we expect data for over 10 000 stars of spectral type earlier than F8 in the direction of nearby OB associations of which around 7000 are located in the direction of Sco OB2. The data will be analyzed for membership. The membership lists will greatly facilitate future extension of the $v \sin i$ data as well as searches for binaries. In addition to proper motions HIPPARCOS will also provide information on duplicity for binaries with separations of more than 0.1 arcsecond.

On the theoretical side it will be very useful to calculate the expected effects of stellar rotation on Walraven colours. As a first step the calculations of CTC can be used. We have used the Roche model for rotating stars throughout this paper. This model is a very simple approximation to reality and introduces a specific break-up velocity. In the case of non-uniformly rotating stars it is not clear that a break-up velocity exists and the observed equatorial velocity depends very much on the internal distribution of angular momentum. For a given mass a stronger degree of concentration of angular momentum towards the centre of the star leads to a lower observed v_e (see e.g., Bodenheimer 1971). So a consequence may be that there are many more low $v \sin i$ stars than would be expected on the basis of uniformly rotating models. Furthermore, the displacement of stellar models in the HR-diagram changes and becomes more parallel to the main-sequence if the central concentration of angular momentum increases. In highly differentially rotating models the stellar surface can develop a cusp at the poles and large variations in surface gravity may result. The present measurements of $v \sin i$ still depend on the Roche model for rotating stars (for the rapid rotators) and on the correctness of approximating the atmosphere of a rotating star as plane-parallel pieces of Kurucz atmospheres on the surface of a rotating star. In order not to bias measurements of $v \sin i$ better theoretical models are needed in which the

atmospheric structure follows from the parameters of the rotating star.

Finally, real constraints on the star formation process can only be obtained if these data can be compared to models that make detailed predictions of the distribution of rotational velocities, taking the star formation process into account. The models should take into account the early phases of star formation. In these phases the details of the (possible) magnetic braking process may determine whether a binary star is formed or not (e.g., Mouschovias 1991). Subsequently the angular momentum history of the protostellar phase should be taken into account. Besides the angular momentum history, the origin of stellar masses and their radii should also be looked into, as these determine the observed value of $v \sin i$.

Acknowledgements. We thank H. Hensberge, R.S. Le Poole and P.T. de Zeeuw for many fruitful discussions that greatly helped improve this paper. M. David and E.J. de Geus are acknowledged for their help in gathering and reducing the data. We thank R.J. Truax for kindly providing the CTC models in digital form. M. Perryman and J. Lub are acknowledged for comments that helped improve the final version of this paper. This research was supported (in part) by the Netherlands Foundation for Research in Astronomy (NFRA) with financial aid from the Netherlands organization for scientific research (NWO). W.V. carried out this research in the framework of the project Service Centres and Research Networks, initiated and financed by the Belgian Federal Scientific Services (DWTC/SSTC).

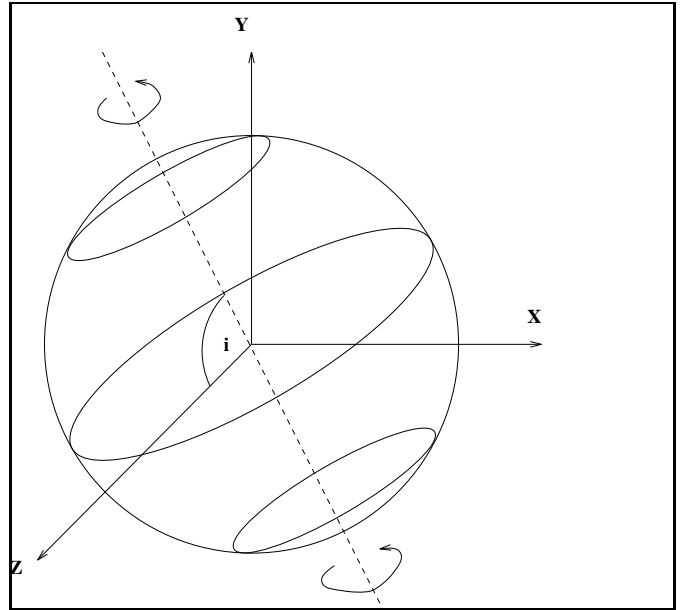


Fig. 15. Frame of reference, attached to a rotating star, that is to be used in deriving the rotational broadening function. The Z-axis points towards the observer.

Appendix A: The Rotational Broadening Function

Following Tassoul (1978), we derive here the rotational broadening function $A(x)$ for different limb-darkening laws. A rectangular frame of reference is used with its origin at the centre of the star. The Z -axis points towards the observer, and the Y -axis lies in the plane passing through the axis of rotation and the line of sight. It is assumed that the star is rotating uniformly, and that its observed disc is a circle of radius R (see also Fig. 15). For convenience: $x = X/R$ and $y = Y/R$.

According to assumption C of the classical model for rotating stars the line profiles in the spectrum of a star are constant over its surface and are given by:

$$I(x, y; \lambda - \lambda_c) = r(\lambda - \lambda_c) I_0(x, y), \quad (\text{A1})$$

where $I_0(x, y)$ is the continuum intensity emergent at the stellar surface at position (x, y) and $r(\lambda - \lambda_c)$ is the ratio of the intensity in the spectral line to the continuum intensity. The rotationally broadened spectral line is then defined as:

$$\bar{r}(\lambda - \lambda_c) = \int_{-1}^{+1} r(\lambda - \lambda_c - \lambda_c x \frac{v \sin i}{c}) A(x) dx. \quad (\text{A2})$$

Here $xv \sin i = -v_z$ and $A(x)$ is the rotational broadening function given by:

$$A(x) = \frac{\int_0^{(1-x^2)^{1/2}} I_0(x, y) dy}{\int_{-1}^{+1} dx \int_0^{(1-x^2)^{1/2}} I_0(x, y) dy}. \quad (\text{A3})$$

To calculate $A(x)$ a limb-darkening law has to be adopted. In Table 8 we list three forms for the limb-darkening law and the corresponding rotational broadening functions. In the first column the limb-darkening law is listed and in the second column the rotational broadening function. In the limb-darkening laws $\mu = \cos \theta = \sqrt{1 - (x^2 + y^2)}$, where θ is the angular distance from the centre of the disc. The limb-darkening parameters are u , p , q , r , and s .

The first two limb-darkening laws are the well known linear and quadratic approximation to limb-darkening and the third law is the square-root approximation proposed by Díaz-Cordovés & Giménez (1992).

If $S(\lambda)$ is the intrinsic spectrum, then the rotationally broadened spectrum $S_r(\lambda)$ is given by:

$$S_r(\lambda) = \int_{-1}^{+1} S\left(\lambda - \lambda x \frac{v \sin i}{c}\right) A(x) dx, \quad (\text{A4})$$

or, substituting $z = \lambda x \frac{v \sin i}{c}$:

$$S_r(\lambda) = \int_{-\lambda_r}^{+\lambda_r} S(\lambda - z) \frac{1}{\lambda_r} A\left(\frac{z}{\lambda_r}\right) dz, \quad (\text{A5})$$

where $\lambda_r = \lambda \frac{v \sin i}{c}$.

7.1. The Rotational Broadening Function in $\ln \lambda$ -Space

Rotational broadening of the spectrum depends on wavelength. This can be seen in the convolution integral in Eq. (A5) which is used to calculate $S_r(\lambda)$. The wavelength dependence is in the sense that the rotational broadening function widens as λ increases. This wavelength dependence is absent in $\ln \lambda$ -space (which is almost equivalent to pixel space for our spectra). By substitution of $\lambda' = \ln \lambda$ into the convolution integral for $S_r(\lambda)$ one finds:

$$S'_r(\ln \lambda) = \int_{-\ln(1+\frac{v \sin i}{c})}^{-\ln(1-\frac{v \sin i}{c})} S'(\ln \lambda - x') A'(x') dx', \quad (\text{A6})$$

where $S'(\ln \lambda)$ is the spectrum and $A'(x')$ the rotational broadening function in $\ln \lambda$ -space.

The rotational broadening functions in $\ln \lambda$ -space for the different limb darkening laws can be found from the rotational broadening functions in λ -space (listed above) as follows:

$$A'(x') = \frac{e^{-x'}}{v \sin i / c} A\left(\frac{1 - e^{-x'}}{v \sin i / c}\right) - \ln\left(1 + \frac{v \sin i}{c}\right) \leq x' \leq -\ln\left(1 - \frac{v \sin i}{c}\right) \quad (\text{A7})$$

This can be derived from the following:

$$S_r(e^{\lambda'}) = S'_r(\lambda') = \int_{-\frac{e^{\lambda'} v \sin i}{c}}^{\frac{e^{\lambda'} v \sin i}{c}} S(e^{\lambda'} - z) \frac{1}{\lambda_r} A\left(\frac{z}{\lambda_r}\right) dz. \quad (\text{A8})$$

Setting $u = z/e^{\lambda'}$, one finds:

$$S'_r(\lambda') = \int_{-\frac{v \sin i}{c}}^{\frac{v \sin i}{c}} S(e^{\lambda'}(1 - u)) \times \frac{1}{v \sin i / c} A\left(\frac{u}{v \sin i / c}\right) du, \quad (\text{A9})$$

since $S(y) = S'(\ln y)$. Substituting $x' = -\ln(1 - u)$ finally yields:

$$S'_r(\lambda') = \int_{-\ln(1+\frac{v \sin i}{c})}^{-\ln(1-\frac{v \sin i}{c})} S'(\lambda' - x') \times \frac{e^{-x'}}{v \sin i / c} A\left(\frac{1 - e^{-x'}}{v \sin i / c}\right) dx'. \quad (\text{A10})$$

7.2. The Width of Rotationally Broadened Lines

At low values of the projected rotational velocity ($v \sin i \lesssim 80 \text{ km s}^{-1}$) the measured width of a line that is not affected by other broadening mechanisms (Apart from thermal and instrumental) can be directly converted into a value of $v \sin i$. In this paper we use metal lines for this purpose and measure their FWHM by fitting Gaussians. This implies a measurement of the second moment of the

Table 8. Rotational broadening functions.

$I_0(\mu)/I_0(1)$	$A(x)$
$1 - u(1 - \mu)$	$\frac{2(1-u)(1-x^2)^{1/2} + \frac{\pi}{2}u(1-x^2)}{\pi(1-\frac{u}{3})}$
$1 - p(1 - \mu) - q(1 - \mu)^2$	$\frac{2(1-p-q)(1-x^2)^{1/2} + \frac{\pi}{2}(2q+p)(1-x^2) - \frac{4}{3}q(1-x^2)^{3/2}}{\pi(1-\frac{2p+q}{6})}$
$1 - r(1 - \mu) - s(1 - \sqrt{\mu})$	$\frac{2(1-r-s)(1-x^2)^{1/2} + \frac{\pi}{2}r(1-x^2) + \frac{3}{\sqrt{2\pi}}(\Gamma(\frac{1}{4}))^2s(1-x^2)^{3/4}}{\pi(1-r-s) + \frac{2\pi}{3}r + \frac{4\pi}{5}s}$

line profile. If the second moment of a Gaussian is σ then the FWHM is given by $2\sqrt{2\ln 2}\sigma$. The second moment of a broadened, intrinsically infinitely sharp line centered on λ_0 is given by:

$$\sigma^2(\lambda_0) = \int_{\lambda_0-\lambda_r}^{\lambda_0+\lambda_r} (\lambda - \lambda_0)^2 \bar{r}(\lambda) d\lambda - \left(\int_{\lambda_0-\lambda_r}^{\lambda_0+\lambda_r} (\lambda - \lambda_0) \bar{r}(\lambda) d\lambda \right)^2, \quad (\text{A11})$$

with $\bar{r}(\lambda)$ in this case given by:

$$\bar{r}(\lambda) = \int_{-\lambda_r}^{+\lambda_r} \delta(\lambda - \lambda_0 - z) \frac{1}{\lambda_r} A\left(\frac{z}{\lambda_r}\right) dz. \quad (\text{A12})$$

Because of symmetry Eq. (A11) reduces to:

$$\sigma^2(\lambda_0) = \int_{-1}^{+1} \lambda_r^2 x^2 A(x) dx. \quad (\text{A13})$$

Note that the last integral contains an integrand in which only terms of the form $x^2(1-x^2)^\nu$ occur, which are all symmetrical around zero. The Beta-function can be given as:

$$B(x, y) = 2 \int_0^1 t^{2x-1} (1-t^2)^{y-1} dt \quad (\text{Re}(x) > 0, \text{Re}(y) > 0). \quad (\text{A14})$$

So one can easily evaluate σ^2 using this expression for the Beta-function and the relation between the Beta function and the Gamma-function. For linear limb-darkening the result is:

$$\sigma^2(\lambda_0) = \lambda_r^2 \left(\frac{\frac{3}{4} - \frac{7}{20}u}{3-u} \right) \quad (\lambda_r = \lambda_0 \frac{v \sin i}{c}). \quad (\text{A15})$$

The results for quadratic and square-root limb-darkening are:

$$\sigma^2(\lambda_0) = \lambda_r^2 \left(\frac{\frac{3}{2} + \frac{1}{10}p - \frac{6}{5}q}{6 - 2p - q} \right), \quad (\text{A16})$$

$$\sigma^2(\lambda_0) = \lambda_r^2 \left(\frac{\frac{15}{4} - \frac{7}{4}r - \frac{13}{12}s}{15 - 5r - 3s} \right). \quad (\text{A17})$$

The ECHELEC spectra that are being analyzed are recorded in $\ln \lambda$ -space and in that case one can show that the general equation for the second moment σ' is:

$$(\sigma')^2 = \int_{-1}^{+1} \ln^2\left(1 - \frac{v \sin i}{c} y\right) A(y) dy - \left(\int_{-1}^{+1} \ln\left(1 - \frac{v \sin i}{c} y\right) A(y) dy \right)^2. \quad (\text{A18})$$

The two integrals in the equation cannot be calculated straightforwardly. However, in the limit $v \sin i / c \ll 1$ the integrals reduce to the same form as for σ but without the dependence on wavelength. Since the method is specifically applied in cases of low values of $v \sin i$ the approximation should hold when determining $v \sin i$ from the FWHM of the metal lines. For B3–B5 stars ($T_{\text{eff}} \approx 15000\text{K}$) the values of u , p , q , r , and s in the Strömgren v -band at $\log g = 4.5$ are 0.408, 0.159, 0.324, -0.102 , and 0.723, respectively (taken from Díaz-Cordovés et al.1995). This leads to the following values for the coefficients of λ_r in Eqs. (A15), (A16) and (A17); 0.234, 0.210, and 0.236. This illustrates that the derived values of $v \sin i$ are not very sensitive to the choice of limb-darkening law.

Appendix B: Fourier Filtering of Template and Target Spectrum

As mentioned in Sect. 3.2 it is necessary to filter both the target and the broadened template spectrum before comparing the two. The filtering is done in Fourier-space

and the high-pass filter is constructed as follows. The information relevant to the rotation of a star can be found in its spectrum on spatial scales $\sim 2v\sin i$ (in km s^{-1}). All components in the spectrum with longer spatial scales than this value carry essentially no information on $v\sin i$ and can be filtered out. So based on the highest value in the $v\sin i$ search interval one can construct the high-pass filter in Fourier-space. This filter is a step function with its edge tapered by a narrow Gaussian. The edge of the filter is placed at the frequency corresponding to the upper limit of the tested $v\sin i$ values. In practice two extra frequencies below the edge value are retained. This is to insure that one does not throw away too much information. After filtering, the comparison between template and target is done as described in Sect. 3.2.

The data do not contain a number of points equal to a power of two as required by the FFT routine used. So in practice in order to avoid creating large discontinuities in the data by zero padding we connect the endpoints in the data by a straight line and subtract that line from the data. The endpoints are often very noisy so we first discard the outer 10 points at each end. Components with a spatial wavelength smaller than $\sim 260 \text{ km s}^{-1}$ were never filtered out in order to avoid being dominated by small mismatches between template and target spectrum. Signal to noise considerations also lead us to throw out 40 extra pixels at both edges of every spectral order (containing 500 pixels in total) before calculating the mean absolute difference between template and target.

Note that before doing the comparison one has to make sure that the template and target spectrum are shifted to the same radial velocity. It turns out that aligning the spectra to within one pixel is sufficiently accurate (see Appendix C). This can be done by eye.

Appendix C: The Effects of Gravity- and Limb-Darkening on Template Broadening

As discussed in Sect. 3.2 we expect gravity- and limb-darkening to have more severe effects when one uses template broadening to derive $v\sin i$. We investigated this by generating synthetic data from the ab initio models by CTC. We took the models of the He I $\lambda 4026$ line and the H γ line and constructed synthetic 'spectral orders' with the same characteristics as an ECHELEC spectral order. The continuum was taken to be constant (normalized flux 1) and Poisson noise was added artificially. The artificial spectral order is calculated in $\ln \lambda$ -space because the models are given as a function of wavelength. Models with low values of $v\sin i$ were used as templates. This investigation was done for B3 and B9 models in order to compare results for different spectral types.

An example is shown in Fig. 16 for the He I $\lambda 4026$ line. In both cases the target spectrum is that of a star with $w = 0.8$ and $i = 90^\circ$. The corresponding values of $v\sin i$ are

250 km s^{-1} and 213 km s^{-1} , respectively, for the B3 and B9 target. The noise in the target spectra corresponds to a signal to noise ratio of 250. This is a typical value for order 142. The templates were non-rotating models in both cases. The template broadening technique applied in these two cases yields values for $v\sin i$ of 240 km s^{-1} for the B3 target and 180 km s^{-1} for the B9 target. The broadened template spectra in Fig. 16 correspond to these values. Also plotted in Fig. 16 are the same model spectra without the noise in order to show the actual differences between the broadened template and the target. In both cases one can see that the He I $\lambda 4026$ line from the ab initio model is narrower and less deep than the corresponding classically broadened template. This effect is largest for the B9 star. In both cases $v\sin i$ is underestimated by template broadening, but the error for the B3 star is less than 5%. Note that for both spectral types the fit of the noisy broadened template to the noisy data looks good in the high-pass filter case even though the value of $v\sin i$ is wrong.

For the parameters of the example shown ($S/N = 250$, no radial velocity shifts, zero-rotation template), template broadening gives the correct results up to $w = 0.8$ for B3 stars ($v\sin i$ is underestimated by $\sim 5\%$ for $w = 0.8$, $i = 90^\circ$). For B3 stars rotating at $w \geq 0.9$ the value of $v\sin i$ can be underestimated up to 15%. For B9 stars template broadening only works well up to $w = 0.5$ ($v\sin i$ is underestimated by $\sim 10\%$ for $w = 0.5$, $i = 90^\circ$). For higher values of w , $v\sin i$ is underestimated by at least 10–15% and for $w \geq 0.9$ the discrepancies between template broadening and model fitting are so severe that depending on the inclination $v\sin i$ can be overestimated as well as underestimated by $\sim 20\%$.

For the B3 models we investigated the effects of other parameters in the synthetic data. At a lower signal-to-noise ratio in the spectrum ($S/N=100$) the results are not affected. If one introduces small radial velocity shifts of 1 to 2 pixels between template and object the $v\sin i$ values from template broadening are off by 5–8% at the lowest intrinsic $v\sin i$ values. At higher values of $v\sin i$ the results are not affected; it becomes less important at those values to have the phases of template and object match exactly. If one uses a template for which $v\sin i \approx 30 \text{ km s}^{-1}$ the value for the target is underestimated even more. For $w \leq 0.8$ $v\sin i$ is now underestimated by 5–10% and for higher values of w the underestimates can be up to 17%.

The results can be summarized by stating that the $v\sin i$ values for template broadening of the He I $\lambda 4026$ line can be trusted up to $\sim 200 \text{ km s}^{-1}$ for early type B3 stars. For the B9 stars one should only trust template broadening for values of $v\sin i$ less than 120–150 km s^{-1} .

The situation is reversed when using the H γ line. Now it is the B3 stars for which $v\sin i$ is underestimated at low values of w . The value of $v\sin i$ from template broadening can be off by as much as 30% at $w = 0.5$. For B9 stars the value of $v\sin i$ from template broadening can be trusted up to high values of w .

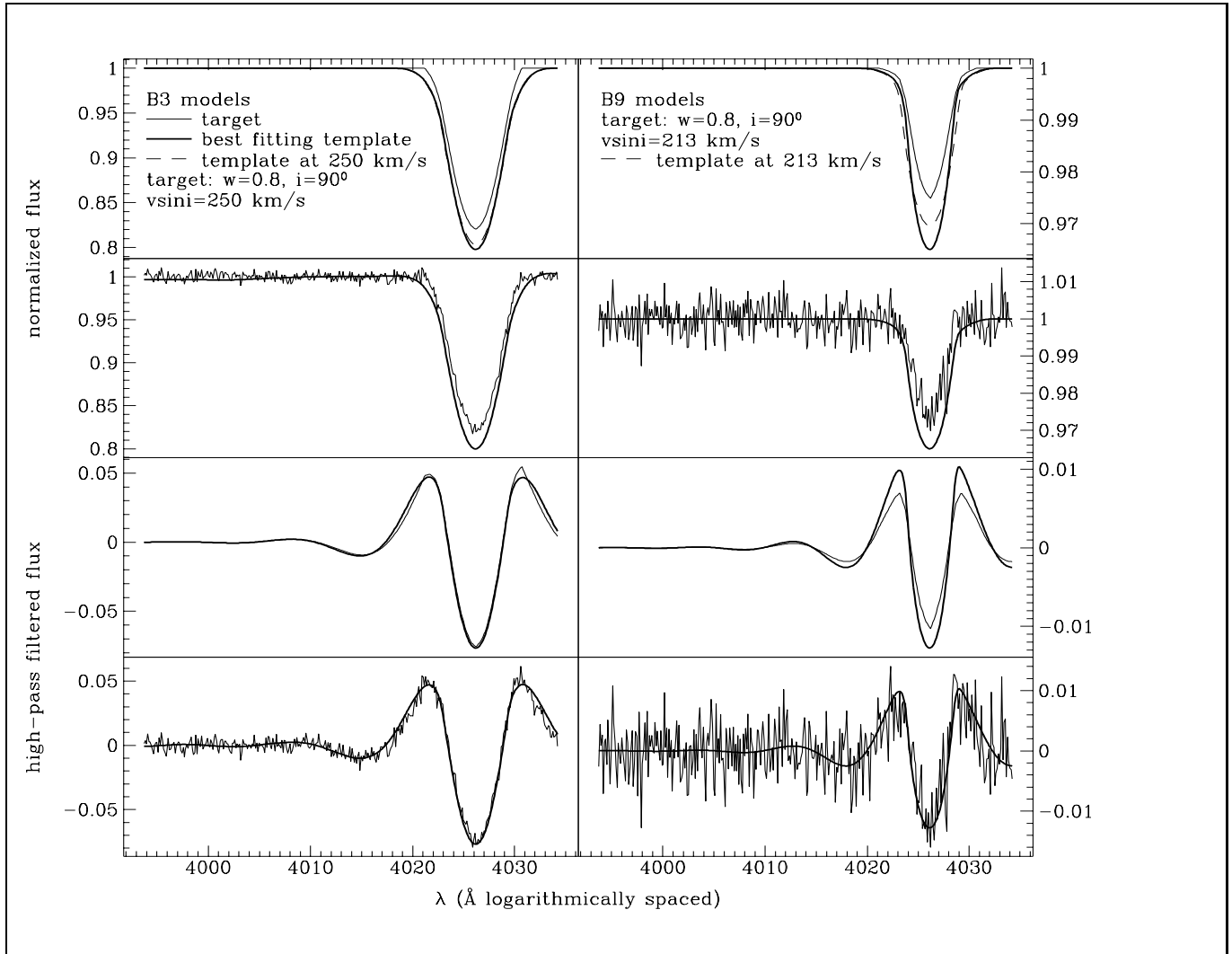


Fig. 16. Example of template broadening applied to synthetic data. The four panels on the left indicate the results for B3 models. The panels on the right show the results for B9 models. The top four panels show a direct comparison between the best fitting broadened template (thick line) and target (thin line). The best fits are based on the *filtered* data. In the top two panels the dashed line is the broadened template corresponding to the real value of $v \sin i$ of the object. The bottom panels show the comparison after high-pass filtering of the data. The same results are shown for synthetic data with and without noise. The noisy data have a signal to noise ratio of 250. In both cases the template is a non-rotating star and the target rotates at 80% of the critical angular velocity. The inclination angle is 90° in both cases. The resulting values of $v \sin i$ are 250 km s^{-1} and 213 km s^{-1} , respectively, for the B3 and B9 targets. The values of $v \sin i$ found from template broadening are 240 km s^{-1} and 180 km s^{-1} , respectively. The broadened templates in this figure correspond to the latter $v \sin i$ values. Note the differences in vertical scale.

The difference in behaviour of He I $\lambda 4026$ and H γ with spectral type is due to a difference in sensitivity to surface gravity. The Balmer lines are most sensitive to surface gravity changes for the early type B-stars. A reduction of the surface gravity causes the wings of the Balmer lines to become less important whereas the line strength in the core remains the same. This effect leads to underestimated $v \sin i$ values and is strongest for the early-type B-stars. The He I $\lambda 4026$ line shows the opposite behaviour and it is the late-type B-stars for which the line is most sensitive

to changes in surface gravity. In this case the whole line becomes weaker and narrower.

The general conclusion is that one should be careful when using template broadening results as soon as $v \sin i$ is larger than $\sim 120\text{--}150 \text{ km s}^{-1}$. Visual inspection of the results is required and one should take the spectral type of the target star into account.

The role of limb-darkening was already discussed in Sect. 3.1. In the simulations we also used the linear limb-darkening law with parameter $u = 0.4$ to calculate the broadened template. The results suggest that the choice

of limb-darkening law does not affect the outcome by much. To investigate this a little further we re-determined $v \sin i$ for a couple of our stars with a different choice of limb-darkening law. The two other forms we tried are the quadratic and square-root approximations to limb-darkening (see e.g., Díaz-Cordovés & Giménez 1992). We took a couple of stars and used a limb-darkening law and parameters appropriate for the spectral type of the stars. The results were not affected and we are confident that the choice of limb-darkening law is not important when using template broadening. The reason is that the differences due to limb-darkening are obscured by the noise in the spectra.

Appendix D: Notes to Table 2

- HD 94650: The He I $\lambda 4026$ line of this star is best fit with a B3 model. The appearance of the Helium lines in order 142 also points to an earlier spectral type.
- HD 95122: The B5 model for He I $\lambda 4026$ gives the best fit.
- HD 100262: This star is a supergiant and the measured $v \sin i$ may actually be determined by macro-turbulence in the atmosphere of this star.
- HD 101947: The value of $v \sin i$ for this star was estimated by eye from its spectrum. This value may also be a measure of macro-turbulence rather than rotation. Note that this star is also classified as G0Ia⁺ (J. Lub, personal communication).
- HD 104878: For this star B9 models were used for He I $\lambda 4026$.
- HD 105382: The best template for the template broadening method was HD 120709, which is a B5 star. Indeed, the star is classified as B6IIIe in the Bright Star Catalogue.
- HD 105580: The best fitting template is HD 132955, a B3V star. The spectrum of this star is clearly not of type B6. Houk and Cowley (1975) classify this star as B3IV.
- HD 107566: The value of $v \sin i$ is taken from Uesugi & Fukuda (1981) and revised downwards by 5% to make the value consistent with the standard system given by SCBWP.
- HD 107696: The best fitting model for He I $\lambda 4026$ is for spectral type B5. The strength of the He I $\lambda 4009$ line is clearly not consistent with spectral type B9. Houk & Cowley (1975) list B7Vn as spectral type for this star.
- HD 108248: HD 149438 (B0V, τ Sco) was used as template.
- HD 108249: This star is a double-lined spectroscopic binary. The model fits were done by direct comparison (without Fourier filtering) of the strongest component to the models. This makes this $v \sin i$ value rather uncertain.
- HD 108257: The He I $\lambda 4026$ line in this star is broader than the models. The value of $v \sin i$ may thus be overestimated.
- HD 108483: The best fitting template is HD 96706, a B2V star. The spectral type listed in Houk (1978) is B2V.
- HD 109787: The value of $v \sin i$ is taken from SCBWP.
- HD 110432: The best fit of the He I $\lambda 4026$ line is for a B5 model.
- HD 111123: HD 149438 was used as template for method 2. HD 11123 is a non-radial pulsator and a β Cephei variable.
- HD 112078: B3 models were used to fit the He I $\lambda 4026$ line. The line profile may be influenced by the presence of a secondary in the spectrum.
- HD 112091: B4 models were used to fit the He I $\lambda 4026$ line.
- HD 112409: B7 models were used to fit He I $\lambda 4026$.
- HD 113703: B3 models were used to fit He I $\lambda 4026$. Houk (1978) lists spectral type B4V for this star.
- HD 113791: Listed as B3V by Houk (1978).
- HD 113902: B7 models were used to fit He I $\lambda 4026$.
- HD 114529: The value of $v \sin i$ for this star was estimated by eye. It may be a double-lined spectroscopic binary.
- HD 116072: B3 models were used to fit He I $\lambda 4026$. The spectral type of this star is B2.5Vn according to the Bright Star Catalogue.
- HD 116226: B5 models were used to fit He I $\lambda 4026$. Houk (1978) gives B5V for the spectral type of this star.
- HD 118716: B3III models were used for method 3. This star is a non-radial pulsator and a β Cephei variable.
- HD 118978: B8 models were used to fit He I $\lambda 4026$.
- HD 119361: B7III models were used to fit He I $\lambda 4026$.
- HD 120324: This star is a non-radial pulsator.
- HD 121190: B7 models were used to fit He I $\lambda 4026$.
- HD 121263: The value of $v \sin i$ may be influenced by the presence of a secondary component in the spectrum.
- HD 124367: B3 models were used to fit He I $\lambda 4026$.
- HD 125238: The stellar He I $\lambda 4026$ line is much deeper than the B3 model line. The value of $v \sin i$ may thus be underestimated.
- HD 125745: B6 models were used to fit He I $\lambda 4026$. The appearance of the Helium lines in order 142 clearly suggests an earlier spectral type.
- HD 126341: This star is a non-radial pulsator and a β Cephei variable.
- HD 126981: B6 models were used to fit He I $\lambda 4026$. The appearance of the Helium lines in order 142 suggests an earlier spectral type.
- HD 127381: HD 126341 (B2IV) was used as template.
- HD 127972: The value of $v \sin i$ is taken from SCBWP.
- HD 128345: B4 models were used to fit He I $\lambda 4026$. Houk (1978) lists the spectral type of this star as B3/B4V
- HD 129056: This star is β Cephei variable.

HD 131625: B9 models were used to fit HeI $\lambda 4026$. The models do not fit well.

HD 132058: HD 126341 was used as template. Houk (1978) lists B2IV as spectral type for HD 132058.

HD 132851: The value of $v \sin i$ was estimated from a visual inspection of the spectrum.

HD 133937: B3 models were used to fit HeI $\lambda 4026$. The appearance of the Helium lines in order 142 clearly suggests an earlier spectral type. Houk (1978) lists the spectral type as B5/B7V.

HD 135876: B6 models were used to fit HeI $\lambda 4026$. The appearance of the Helium lines in order 142 clearly suggests an earlier spectral type. Houk (1978) lists the spectral type as B7V.

HD 136298: B3 models were used to fit HeI $\lambda 4026$. This star is a β Cephei variable.

HD 136664: B3 models were used to fit HeI $\lambda 4026$.

HD 136933: The value of $v \sin i$ was estimated from a visual inspection of the spectrum.

HD 137058: B9 models were used to fit HeI $\lambda 4026$. The models do not fit well.

HD 137432: HD 132955 (B3V) was used as template. The Bright Star Catalogue lists the spectral type of this star as B4Vp.

HD 140784: B4 models were used to fit HeI $\lambda 4026$. The appearance of the Helium lines in order 142 clearly suggests an earlier spectral type. The Bright Star Catalogue lists the spectral type as B7Vn.

HD 141637: B3 models were used to fit HeI $\lambda 4026$. The spectrum shows signs of a secondary component.

HD 142114: The stellar HeI $\lambda 4026$ line is much deeper than the B3 model line. The value of $v \sin i$ may thus be underestimated.

HD 142184: The stellar HeI $\lambda 4026$ line is much deeper than the B3 model line. The value of $v \sin i$ may thus be underestimated.

HD 142629: The value of $v \sin i$ is taken from Uesugi & Fukuda (1981) and revised downwards by 5% to make the value consistent with the standard system given by SCBWP.

HD 142983: The value of $v \sin i$ was estimated from a visual inspection of the spectrum. According to SCBWP this star has a projected rotational velocity of 400 km s^{-1} . However, judging from the spectrum this clearly is not the case. This star is also a non-radial pulsator.

HD 143018: The value of $v \sin i$ is taken from the Bright Star Catalogue and the spectrum was inspected visually to check whether the value listed is reasonable.

HD 143275: B1 models were used to fit HeI $\lambda 4026$ and HD 149438 was used as template for method 2. The B1 model profiles are not really deep enough to fit the data.

HD 144217: HD 149438 was used as template.

HD 144294: The stellar HeI $\lambda 4026$ line is much deeper than the B3 model line. The value of $v \sin i$ may thus be underestimated.

HD 144987: B7 models were used to fit HeI $\lambda 4026$.

HD 145482: The value of $v \sin i$ is influenced by the fact that this star is a double-lined spectroscopic binary.

HD 147084: The value of $v \sin i$ was estimated from a visual inspection of the spectrum.

HD 147165: This star is a β Cephei variable.

HD 147628: B6 models were used to fit HeI $\lambda 4026$. The appearance of the Helium lines in order 142 suggests an earlier spectral type.

HD 147933: The value of $v \sin i$ may be influenced by the presence of a secondary component in the spectrum.

HD 148184: B4 models were used to fit HeI $\lambda 4026$. This star shows emission cores in the Balmer lines present in our spectra.

HD 149757: The value of $v \sin i$ is taken from SCBWP. This star is a non-radial pulsator.

HD 151804: The value of $v \sin i$ was estimated from a visual inspection of the spectrum.

HD 151890: B1 models were used to fit HeI $\lambda 4026$. The value of $v \sin i$ may be influenced by the secondary component in the spectrum.

HD 154204: B4 models were used to fit HeI $\lambda 4026$. The appearance of the Helium lines in order 142 suggests an earlier spectral type. The Bright Star Catalogue lists the spectral type as B6IV.

HD 157042: The value of $v \sin i$ was estimated from a visual inspection of the spectrum. This star is a non-radial pulsator.

HD 157056: This star is a β Cephei variable.

HD 157246: The value of $v \sin i$ is taken from SCBWP. This star is a non-radial pulsator.

HD 158427: The value of $v \sin i$ may be influenced by the presence of a secondary component in the spectrum.

HD 158926: The value of $v \sin i$ was derived from the spectrum by visual inspection. The $v \sin i$ value listed in SCBWP is 190 km s^{-1} . This star is a β Cephei variable.

HD 168905: The stellar HeI $\lambda 4026$ line is much deeper than the B3 model line. The value of $v \sin i$ may thus be underestimated.

HD 171034: HD 126341 was used as template.

References

- Bernacca, P.L., 1970, in *Stellar Rotation*, ed. A. Slettebak, Reidel Dordrecht, p. 227
 Bertiau, F.C., 1958, *ApJ* 128, 533
 Blaauw, A., 1946, Ph.D. Thesis, Groningen University
 Blaauw, A., 1964, *ARA&A* 2, 213

- Blaauw, A., 1978, in *Problems of Physics and Evolution of the Universe*, ed. L. Mirzoyan, Yerevan, USSR, p. 101
- Blaauw, A., 1991, in *The Physics of Star Formation and Early Stellar Evolution*, eds. C.J. Lada & N.D. Kylafis, NATO ASI Series C, Vol. 342, p. 125
- Bodenheimer, P., 1971, *ApJ* 167, 153
- Bodenheimer, P., Ruzmaikina, T., Mathieu, R.D., 1993, in *Protostars and Planets III*, eds. E.H. Levy & J.I. Lunine, The University of Arizona Press, p. 367
- Brand, J., Wouterloot, J.G.A., 1988, *A&AS* 75, 117
- Brown, A.G.A., de Geus, E.J., de Zeeuw, P.T., 1994, *A&A* 289, 101
- Chandrasekhar, S., Münch, G., 1950, *ApJ* 111, 142
- Collins, G.W., II, 1963, *ApJ* 138, 1134
- Collins, G.W., II, Sonneborn, G.H., 1977, *ApJS* 34, 41
- Collins, G.W., II, Truax, R.J., 1995, *ApJ* 439, 860
- Collins, G.W., II, Truax, R.J., Cranmer, S.R., 1991, *ApJS* 77, 541 (CTC)
- Day, R.W., Warner, B., 1975, *MNRAS* 173, 419
- Deutsch, A.J., 1970 in *Stellar Rotation*, ed. A. Slettebak, Reidel Dordrecht, p. 207
- Díaz-Cordovés, J., Giménez, A., 1992, *A&A* 259, 227
- Díaz-Cordovés, J., Claret, A., Giménez, A., 1995, *A&AS* 110, 329
- de Geus, E.J., 1992, *A&A* 262, 258
- de Geus, E.J., de Zeeuw, P.T., Lub, J., 1989, *A&A* 216, 44
- de Geus, E.J., Lub, J., van de Grift, E., 1990, *A&AS* 85, 915
- Gray, D.F., 1992, *The Observation and Analysis of Stellar Photospheres*, Cambridge Astrophysics Series
- Harmanec, P., 1988, *Bull. Astron. Inst. Czechosl.*, 39, 329
- Hensberge, H., van Dessel, E.L., Burger, M., et al. 1990, *The Messenger*, 61, 20
- Hoffleit, D., Jaschek, C., 1982, *The Bright Star Catalogue* (4th revised edition), Yale University Observatory
- Hoffleit, D., Saladyga, M., Wlasuk, P., 1983, *A Supplement to the Bright Star Catalogue*, Yale University Observatory
- Houk, N., Cowley, A.P., 1975, *University of Michigan Catalogue of Two-Dimensional Spectral Types for the HD Stars: Volume 1*, University of Michigan, Ann Arbor
- Houk, N., 1978, *University of Michigan Catalogue of Two-Dimensional Spectral Types for the HD Stars: Volume 2*, University of Michigan, Ann Arbor
- Kurucz, R.L., 1991, *Harvard Preprint* 3348
- Lamers, H.J.G.L.M., Leitherer, C., 1993, *ApJ* 412, 771
- Levato, H., Malaroda, S., Morrell, N., Solivella, G., 1987, *ApJS* 64, 487
- Lucy, L.B., 1974, *AJ* 79, 745
- Lucy, L.B., 1994, *A&A* 289, 983
- Maeder, A., 1971, *A&A* 10, 354
- Mouschovias, T.Ch., 1983, in *Solar and Stellar Magnetic Fields: Origins and Coronal Effects*, IAU Symp. 102, ed. J.O. Stenflo, Dordrecht, Reidel, p. 479
- Mouschovias, T.Ch., 1991, in *The Physics of Star Formation and Early Stellar Evolution*, eds. C.J. Lada & N.D. Kylafis, NATO ASI Series C, Vol. 342, p. 61
- Press, W.H., Teukolsky, S.A., Vetterling, W.T., Flannery, B.P., 1992, *Numerical Recipes in Fortran: The Art of Scientific Computing*, Second Edition, Cambridge University Press
- Rajamohan, R., 1976, *Pramana*, Vol. 7, 160
- Schaller, G., Schaerer, D., Meynet, G., Maeder, A., 1992, *A&AS*, 96, 269
- Siegel, S., Castellan, N.J., Jr., 1988, *Nonparametric Statistics for the Behavioral Sciences*, McGraw-Hill Singapore
- Slettebak, A., 1954, *ApJ* 119, 146
- Slettebak, A., 1955, *ApJ* 121, 653
- Slettebak, A., 1956, *ApJ* 124, 173
- Slettebak, A., 1966a, *ApJ* 145, 121
- Slettebak, A., 1966b, *ApJ* 145, 126
- Slettebak, A., 1968, *ApJ* 151, 1043
- Slettebak, A., Howard, R.F., 1955, *ApJ* 121, 102
- Slettebak, A., Collins, G.W., II, Boyce, P.B., White, N.M., Parkinson, T.D., 1975, *ApJS* 29, 137 (SCBWP)
- Spitzer, L., Jr., 1968, *Diffuse Matter in Space*, Interscience Tracts on Physics and Astronomy
- Straižys, V., Kuriliene, G., 1981, *Ap&SS* 80, 353
- Tassoul, J.-L., 1978, *Theory of Rotating Stars*, Princeton Series in Astrophysics
- Turon, C., Crézé, M., Egret, D., Gómez, A., et al., 1992, *ESA SP-1136*
- Uesugi, A., Fukuda, I., 1981, *Revised Catalogue of Stellar Rotational Velocities*, France: CDS Strasbourg
- Verschueren, W., Brown, A.G.A., Hensberge, H., David, M., Le Poole, R.S., de Geus, E.J., de Zeeuw, P.T., 1996, submitted to *PASP*
- Verschueren, W., et al., 1996, in preparation
- Vio, R., Fasano, G., Lazzarin, M., Lessi, O., 1994, *A&A* 289, 640
- Wolff, S.C., Edwards, S., Preston, G.W., 1982, *ApJ* 252, 322
- de Zeeuw, P.T., Brown, A.G.A., Verschueren, W., 1994, in *Galactic and Solar System Optical Astrometry: Observation and Application*, eds. L.V. Morrison & G.F. Gilmore, Cambridge University Press, p. 215

Table 2a. Projected rotational velocities in Lower Centaurus Crux.

HD	HIC	MK	$v \sin i$	$\sigma(v \sin i)$	v_{br}	$\frac{v \sin i}{v_{\text{br}}}$	Meth.	Mem.	Dupl.
(1)	(2)	(3)	km s ⁻¹	km s ⁻¹	km s ⁻¹	(7)	(8)	(9)	(10)
94650	53272	B6V	400	13	411	0.973	3		*
95122	53556	B7V	152	16	388	0.392	3	RV	*
96706	54327	B2V	11	2	459	0.024	1	CON	
99103	55597	B5	102	4	388	0.263	3		
99264	55657	B2.5IV-V	125	5	411	0.304	3	RV	
99556	55831	B3IV	188	10	411	0.457	3	CON	
100262	56250	A3Ia	30	3	152	0.197	1		*
100841	56561	B9II:	155	17	278	0.558	3		
100929	56606	B2.5IV	23	4	459	0.050	1	CON	
101947	57175	F9Ia	30	10	122	0.246	4		*
102776	57669	B3V	251	9	411	0.611	3	m RV	
103079	57851	B4V	47	7	401	0.117	1,2	M	
103884	58326	B3V	149	8	411	0.363	2,3	M CON	
103961	58379	B8III	60	7	288	0.208	1,2		
104841	58867	B2IV	25	2	459	0.054	1	m SB1	
104878	58884	A0V	225	30	350	0.643	3	RV	*
105382	59173	B2IIIne	75	13	303	0.248	1,2	M RV	*
105435	59196	B2IVne	298	14	411	0.725	3	M RV	
105580	59266	B6V	44	8	411	0.108	1,2		*
105937	59449	B3V	129	6	411	0.314	3	M RV	
106490	59747	B2IV	135	6	411	0.328	3	M CON	
106983	60009	B2.5V	65	9	459	0.142	1,2	M	
107566	60320	Am	114	11	357	0.319	4		*
107696	60379	B9V	382	40	388	0.985	3	m	*
108248	60718	B0.5IV	88	5	504	0.175	2	SB1	*
108249		B1V	150	20	491	0.305	3	RV	*
108250		B4V	131	6	401	0.327	3	SB1	
108257	60710	B3Vn	298	12	411	0.725	3	M CON	*
108483	60823	B3V	169	12	459	0.368	2	M RV	*
109026	61199	B5V	188	10	401	0.469	3	M RV	
109668	61585	B2IV-V	114	11	459	0.248	2	M RV	
109787	61622	A2V	280	28	365	0.767	4		*
110304	61932	A1IV	79	3	337	0.234	2	RV	
110432	62027	B2pe	388	42	388	1.000	3	RV	*
110879	62322	B2V	139	6	411	0.338	3	m RV	
110956	62327	B3V	26	4	411	0.063	1	M RV	
111123	62434	B0.5III	40	5	401	0.100	12	M RV	*
112078	63007	B4Vn	298	27	411	0.725	3	M RV	*
112091	63005	B5Vne	242	10	401	0.603	3	M	*
112092	63003	B2IV-V	34	3	459	0.074	1	M CON	

Table 2a. (Continued)

HD	HIC	MK	$v \sin i$	$\sigma(v \sin i)$	v_{br}	$\frac{v \sin i}{v_{\text{br}}}$	Meth.	Mem.	Dupl.
(1)	(2)	(3)	km s ⁻¹	km s ⁻¹	km s ⁻¹	(7)	(8)	(9)	(10)
112409	63210	B8V	164	25	373	0.440	3		*
113703	63945	B5V	140	7	411	0.341	3	M	*
113791	64004	B1.5V	15	2	475	0.032	1	M SB1	*
113902	64053	B8V	281	46	373	0.753	3		*
114529	64425	B8V	250	25	363	0.689	4	RV	*
115823	65112	B6V	42	5	381	0.110	1	M RV	
115846	65181	B3V	168	7	411	0.409	3		
116072		B4V(V?)	223	11	411	0.543	3		*
116087	65271	B3V	223	11	411	0.543	3	M CON	*
116226	65303	B6IV	215	22	388	0.554	3		*
118716	66657	B1III	114	15	377	0.302	2,3	M RV	*
118978	66849	B9IV	182	29	363	0.501	3	m	*
124471	69763	B1.5III	38	4	377	0.101	1	RV	*

Table 2b. Projected rotational velocities in Sco OB2-1.

HD	HIC	MK	$v \sin i$	$\sigma(v \sin i)$	v_{br}	$\frac{v \sin i}{v_{\text{br}}}$	Meth.	Mem.	Dupl.
(1)	(2)	(3)	km s ⁻¹	km s ⁻¹	km s ⁻¹	(7)	(8)	(9)	(10)
151804	82493	O9e	75	15	508	0.148	4		*
152234	82676	B0.5Ia	90	11	400	0.225	1	RV	*
152236	82671	B1Iae	75	2	373	0.201	1		
157042	85079	B2IIIne	275	30	364	0.755	4		*
157246	85267	B1Ib	230	23	382	0.602	4	RV	*
158408	85696	B2IV	28	4	459	0.061	1	RV	*
158427	85792	B2Vne	295	19	411	0.718	3	RV	*
158926	85927	B1.5IV+...	150	20	475	0.316	4	SB2	*
163685	88012	B3II/III	13	3	326	0.040	1		
165024	88714	B2Ib	108	3	329	0.328	1	RV	
166596	89290	B2.5III	212	9	326	0.650	3		
167128	89605	B3IIIpe	47	6	326	0.144	1	RV	
167756	89726	B0.5Ia	76	6	400	0.190	1		
168905	90200	B2.5Vn	248	12	411	0.603	3	CON	*
169467	90422	B3IV	23	3	411	0.056	1	RV	
170523	90853	B3III	11	2	326	0.034	1	SB1	
171034	91014	B2III/IV	107	10	459	0.233	2	CON	*
172910	91918	B2V	12	2	459	0.026	1	RV	

Table 2c. Projected rotational velocities in Upper Centaurus Lupus.

HD	HIC	MK	$v \sin i$	$\sigma(v \sin i)$	v_{br}	$\frac{v \sin i}{v_{\text{br}}}$	Meth.	Mem.	Dupl.
(1)	(2)	(3)	km s ⁻¹	km s ⁻¹	km s ⁻¹	(7)	(8)	(9)	(10)
119361	66984	B8III	139	18	296	0.470	3		*
120307	67464	B2IV	65	6	459	0.142	1,2	M	SB1
120324	67472	B2IV-Ve	130	9	459	0.283	2,3	M	RV
120640	67663	B2Vp	21	3	459	0.046	1		CON
120709	67669	B5	8	3	388	0.021	1	M	RV
120710		B9V	175	28	350	0.500	3	m	SB1
120955	67786	B4IV	40	2	401	0.100	1	M	SB1
121190	67973	B8V	240	32	373	0.643	3	m	*
121263	68002	B2.5IV	128	6	411	0.311	3		SB2 *
121743	68245	B2IV	79	7	459	0.172	2	M	RV
121790	68282	B2IV-V	124	7	459	0.270	2	M	CON
122980	68862	B2V	15	3	459	0.033	1	M	RV
124367	69618	B4Vne	323	34	411	0.786	3	m	CON *
125238	69996	B2.5V	222	11	411	0.540	3	m	CON *
125745	70243	B8V	271	26	381	0.711	3		*
125823	70300	B2V	15	2	459	0.033	1	M	RV
126341	70574	B2IV	15	2	459	0.033	1		RV *
126981	70915	B8Vn	320	40	381	0.840	3	m	*
127381	71121	B2III	69	10	364	0.190	2		*
127971	71353	B6V	177	21	381	0.465	3		*
127972	71352	B1Vn+...	260	26	491	0.530	4	M	RV *
128345	71536	B5V	186	11	401	0.464	3		CON *
129056	71860	B1.5III	16	3	377	0.042	1	M	RV *
129116	71865	B2.5V	129	6	411	0.314	3	M	CON
130807	72683	B5IV	27	3	388	0.070	1	M	RV
131120	72800	B7II/III	57	6	296	0.193	1	m	CON
131562	73095	A2III	57	3	307	0.186	2		RV
131625	73049	A0V	183	12	350	0.523	3		SB2 *
132058	73273	B2III	92	6	364	0.253	2	M	RV *
132200	73334	B2IV	32	3	459	0.070	1	M	RV
132851	73566	A4IV	120	18	350	0.343	4		*
132955	73624	B3V	8	1	411	0.019	1	M	RV
133937	74100	B7V	402	13	411	0.978	3	M	RV *
133955	74117	B3V	135	14	411	0.328	3	M	RV
134481	74376	B9V	175	28	350	0.500	3		*
134687	74449	B3IV	13	3	411	0.032	1	m	SB1
135876	74950	B9V	118	9	381	0.310	3		SB2 *
136298	75141	B1.5IV	193	9	411	0.470	3	M	RV *
136504	75264	B2IV-V	41	6	459	0.089	1	m	SB2
136664	75304	B4V	177	17	411	0.431	3	M	RV *
136933	75439	Ap...	35	5	362	0.097	4		*
137058	75501	A0V	268	58	350	0.766	3		*
137432	75647	B5V	77	12	411	0.187	2	M	SB1 *
138769	76371	B3IVp	67	6	411	0.163	1	M	RV

Table 2d. Projected rotational velocities in Upper Scorpius.

HD	HIC	MK	$v \sin i$	$\sigma(v \sin i)$	v_{br}	$\frac{v \sin i}{v_{\text{br}}}$	Meth.	Mem.	Dupl.
(1)	(2)	(3)	km s ⁻¹	km s ⁻¹	km s ⁻¹	(7)	(8)	(9)	(10)
139365	76600	B2.5V	134	8	459	0.292	2	M	SB2
140008	76945	B5V	11	3	388	0.028	1	M	SB2
140784	77286	B8V	401	40	401	1.000	3		*
141556	77634	B9.5III-IV	8	2	325	0.025	1		SB2
141637	77635	B1.5Vn	227	12	411	0.552	3	M	RV *
142096	77811	B3V	146	5	411	0.355	3	M	SB2
142114	77840	B2.5Vn	240	12	411	0.584	3	M	CON *
142184	77859	B2V	255	17	411	0.620	3	M	CON *
142629	78105	A3V	81	10	368	0.220	4		*
142669	78104	B2IV/V	98	8	459	0.214	2	M	SB1
142883	78168	B3V	14	2	411	0.046	1	M	SB2
142983	78207	B8Ia/Iab	40	10	187	0.214	4		*
142990	78246	B5V	178	22	388	0.459	3	M	RV
143018	78265	B1V+...	100	15	491	0.204	4	M	SB2 *
143118	78384	B2.5IV	191	8	411	0.465	3	M	RV
143275	78401	B0.2IV	148	8	489	0.303	2,3	M	SB1 *
144217	78820	B0.5IV	91	8	504	0.181	2	M	SB2 *
144218	78821	B2V	56	8	459	0.122	1,2	M	RV
144294	78918	B2.5Vn	252	7	411	0.613	3	M	RV *
144470	78933	B1V	100	6	491	0.204	2	M	CON
144844	79098	B9V	10	2	350	0.029	1	M	SB2
144987	79199	B8V	240	32	373	0.643	3		RV *
145482	79404	B2V	174	10	459	0.379	2	M	SB2 *
145483	79399	B9V	225	30	350	0.643	3	M	
145502	79374	B2IV	162	8	411	0.394	3	M	SB1
146624	79881	A0V:	41	3	362	0.113	1,2		
147084	80079	A4II/III	10	5	261	0.038	4	M	RV *
147165	80112	B1III	56	15	390	0.144	1	M	SB2 *
147628	80390	B8V	170	12	381	0.446	3		RV *
147933	80473	B2V	196	10	411	0.477	3	M	RV *
147934		B2V	223	11	411	0.543	3	M	RV
148184	80569	B2Vne	148	15	401	0.369	3	M	SB1 *
148703	80911	B2III-IV	70	8	364	0.192	2	M	RV
149438	81266	B0V	10	2	515	0.019	1	M	RV
149757	81377	O9.5V	320	32	601	0.532	4	M	CON *
151890	82514	B1.5IV+...	180	9	411	0.438	3	M	SB2 *
151985	82545	B2IV	52	5	459	0.113	1,2	M	RV
154090	83574	B2Iab	78	2	314	0.248	1		
154204	83567	B7IV/V	372	24	401	0.928	3		*
155889	84444	B1/B2Ib/II	38	4	361	0.105	1		
157056	84970	B2IV	31	3	459	0.068	1	M	RV *